Autoclaved Aerated Concrete Tile Vaults for Lightweight Floor Systems

by

Grace Anne Jagoe

B.S. Civil Engineering
University of Notre Dame, 2020

SUBMITTED TO THE DEPARTMENT OF CIVIL AND ENVIRONMENTAL ENGINEERING IN PARTIAL FUFILLMENT OF THE REQUIREMENTS FOR THE DEGREE OF

MASTER OF ENGINEERING IN CIVIL AND ENVIRONMENTAL ENGINEERING

AT THE

MASSACHUSETTS INSTITUTE OF TECHNOLOGY

June 2021

Signature of Author .....
Department of Civil and Environmental
May 14, 2021

Certified by .....
John Ochsendorf
Class of 1942 Professor of Civil and Environmental Engineering and Architecture
Thesis Supervisor

Accepted by .....
Colette L. Heald
Professor of Civil and Environmental Engineering
Chair, Graduate Program Committee

Autoclaved Aerated Concrete Tile Vaults for Lightweight Floor Systems

By

Grace Anne Jagoe

Submitted to the Department of Civil and Environmental Engineering on May 14, 2021, in partial fulfillment of the requirements for the Degree of Master of Engineering in Civil and Environmental Engineering

Abstract

In the construction of multistory buildings, the reinforced concrete flat slab is a preferred floor system in part due to ease of formwork construction, which does not require skilled labor. However, the flat slab carries load primarily in bending, forcing much of the concrete section to crack because of the low tensile capacity of concrete. Thus, up to 61% of the material in the floor system may contribute to the structural weight without carrying substantial load. Material inefficiencies such as this are expensive not only from a cost perspective, but also from an environmental perspective. The embodied carbon of a structure, the emissions of CO_2e associated with material consumption, is directly proportional to the weight of material. With the demand for new construction on the rise, the urgency for more sustainable buildings necessitates more efficient use of material to reduce the embodied carbon associated with structural floor systems.

This thesis explores the use of tile vaults as permanent formwork for concrete floor systems. The proposed system is lighter weight than traditional flat reinforced concrete slabs due to the structural efficiency of material: concrete carries load to the supports in compression and steel resists the outward thrust in tension. Drawing upon traditional masonry construction techniques, a square groin vault can be built using lightweight autoclaved aerated concrete (AAC) tiles and fast-setting mortar without the need for complex falsework. The vaulted floor is designed using equilibrium calculations for various load cases to ensure stability throughout the lifespan of the structure. Alternative geometries and concrete mixes are studied to optimize the system, resulting in a vaulted floor with 67% reduction in structural weight and 61% reduction in embodied carbon compared to a conventional concrete flat slab. Finally, experimental testing validates three possible mortars for the use with AAC tiles for the construction of efficient vaulted floor systems.

Thesis Supervisor: John Ochsendorf
Title: Class of 1942 Professor of Civil and Environmental Engineering and Architecture

Acknowledgments

First, I would like to thank my advisor John Ochsendorf for his guidance throughout this year. I am grateful for the opportunity to learn from his work in the study of masonry structures and to investigate the applications of the principles of historic structures to contemporary structural design.

I thank Steve Rudolph and Chris Dewart for their generosity in assisting me with material testing. Thank you, Steve for your time and guidance in designing and carrying out experiments in the lab and thank you, Chris, for helping me with the preparation of my specimens.

I also would like to thank Stephanie Baez for dedicating her UROP to helping further my thesis through research of alternative concrete mixes and sizing of structural members.

Thank you to Caitlin Mueller, Josephine Carstensen, and Bill Baker for introducing me to a new world of structural designers, projects, and methods and for inciting in me an interest in more efficient structural design. Thank you to Demi Fang for the use of her Grasshopper script and for helping me troubleshoot my model.

To my fellow peers in the M. Eng. Program, thank you for fostering a sense of community within our cohort this year despite the separation induced by the COVID-19 pandemic. In particular, I am grateful to Sabrina Gaitan for our close collaborations in classes and on our theses and for our continued friendship throughout this year.

Lastly, I would like to thank my entire family, especially my parents, for their loving support throughout this year. My successful completion of this program would not have been possible without your prayers and encouragement.

Table of Contents

List of Figures

List of Tables

Chapter 1 : Introduction

1.1 Motivation

The construction industry today is faced with two conflicting demands: the need for new construction and the need for decreased carbon consumption. It is estimated that between 2015 and 2050, there will be over two trillion square feet of new construction and renovations worldwide, due to the rapid growth of cities (King 2017). Each new square foot of construction, however, dramatically impacts the environment, as the energy consumed throughout the construction process largely contributes to greenhouse gas emissions. In fact, the building sector in the United States is responsible for 40% of primary energy use and associated greenhouse gas (GHG) emissions (DOE 2015b). In order to sustain the demand for new construction, engineers and builders must find ways to design and build less energy-intensive structures.

The energy consumption of buildings has been the concern of the green building movement since its genesis in the 1970s and is responsible for the push towards increasingly efficient buildings (King 2017). The apparent solution to preventing new construction from causing future harm to the environment would seem to be zero-energy buildings, which according to the United States Department of Energy are "energy-efficient [buildings] where, on a source energy basis, the actual annual delivered energy is less than or equal to the on-site renewable exported energy" (DOE 2015a). However, the term "zero-energy" only speaks to the operational energy of a building during its lifespan and fails to address embodied energy.
The operational energy of building is the energy consumed while the building is in use; heating, cooling, ventilation, and lighting systems all contribute to the operational energy of a structure. The embodied energy is the energy that is consumed before the operational phase in the lifespan of a building. Embodied energy comes from extracting raw resources, processing materials, manufacturing and assembling components, constructing the building, and all required transportation throughout the process (Ibn-Mohammed et al. 2013). Rather than speaking about operational and embodied energy, it is useful instead to use the terms operational and embodied carbon, which are the carbon dioxide (and carbon dioxide equivalent, CO_2e) emissions associated with those energy consumptions. As operational efficiency improves through the push towards zero-energy structures, the percentage of carbon dioxide emissions of a structure that

comes from embodied carbon grows. As illustrated in Figure 1-1, 100% of the total energy in net zero buildings comes from embodied carbon, the effects of which cannot be ignored (King 2017).

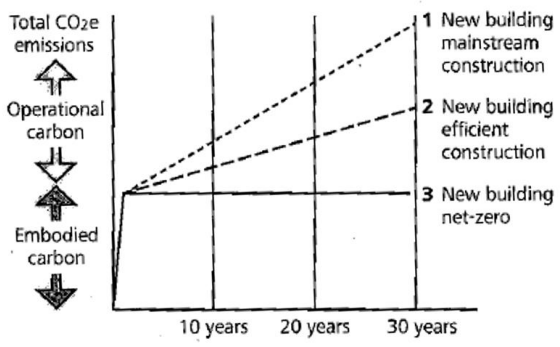

Figure 1-1: Breakdown of CO_2e emissions (King 2017)

As previously mentioned, many sources contribute to the total embodied carbon of a building and a life cycle analysis is required to fully account for all the carbon emissions throughout the lifespan of a building. This study will focus on the embodied carbon from structural material, which can be calculated by multiplying the weight of each type of material by its corresponding embodied carbon coefficient (ECC). The ECC is an empirically derived value used to convert the weight of structural material to weight of equivalent embodied carbon. Because of the linearly proportional relationship between structural weight and embodied carbon, the conclusion that decreasing structural weight reduces embodied carbon is valid. However, as different materials can have drastically different ECCs – for example, steel and concrete – a deeper look at the contribution of each material to the total weight is necessary.

In most buildings, the majority of the structural material is concentrated in the floor systems, which are also the greatest contributors to the total embodied carbon of a building (De Wolf et al. 2016). Thus, in an effort to reduce the total material consumption and embodied carbon, the obvious choice is to begin with optimizing the floor systems. Optimized floors systems can have cascading effects in the design of the rest of the structure. If the floors are reduced in weight, columns and foundations will also require less material and the design earthquake loads will be lower due to the reduced seismic weight of the structure.

Concrete slabs are one of the most common floors systems, as they are easy to construct and required no specialized labor. Although simple, this system is not the most efficient. Floor

slabs carry loads in bending, where, under gravity loads, the top of the cross section goes into compression and the bottom goes into tension. The bottom of the section cracks, due to the limited tensile capacity of concrete, rendering that section unable to transfer load and therefore underutilized (Hawkins 2019). Figure 1-2 adapted from Hawkins (2019) shows the stress distribution at the theoretical point of failure of a 300 mm (11.8 in) thick one-way slab which spans 10 m (32.8 ft). Carrying a uniform load of 10 kN/m^2 (208.9 lb/ft^2) in bending, the resulting stresses are highly non-uniform; stresses are concentrated at the upper edge of the section at midspan. 61% of the concrete is cracked so the average stress in the slab is only 9.4% of the design strength (Hawkins 2019).

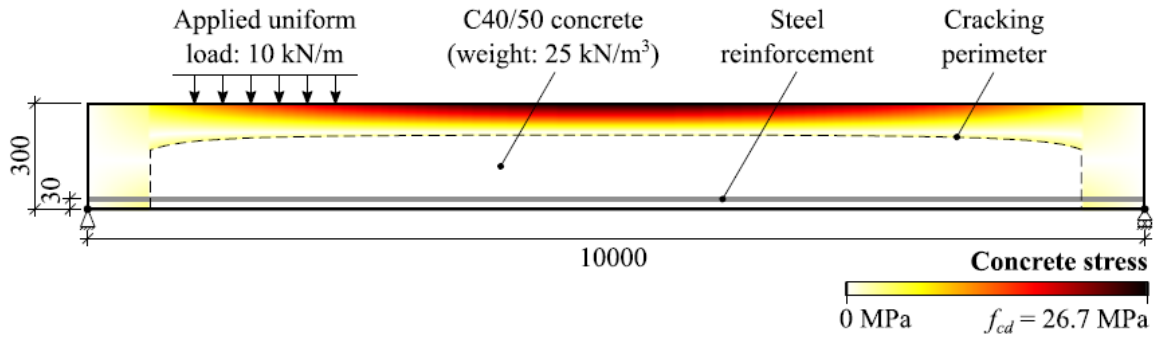

Figure 1-2: Stresses in a one-way slab (Hawkins 2019)

To carry the load in bending means that over half of the self-weight of the slab comes from material that is not being structurally utilized (Hawkins 2019). A more efficient method, engaging more of the concrete cross-section, is to carry the load axially. Arches provide a solution to this requisite: applied loads induce internal compressive stresses rather than flexural stresses. A vaulted system carries load more efficiently and eliminates underutilized material, making it a viable option for a low-weight, low-embodied carbon floor system (Barentin 2020). Recent scholarly interest in the possibilities for vaulted floor systems are summarized in the literature review.

1.2 Literature Review

The literature relevant to the design and construction of masonry vaults includes equilibrium analysis of masonry and historic building techniques as well as modern implementations of vaulted floor systems and lightweight materials for tile vaulting.

1.2.1 Equilibrium Analysis of Masonry

Masonry structures are highly indeterminate, and analysis of masonry relies on plastic theory to safely design structures. An elastic solution would provide an exact state of stress through the structure for given loads; however, this method requires knowledge of the exact boundary conditions, which are unknown, and relies on the law of elastic deformations, which does not easily apply to heterogeneous stone masonry. Therefore, it is impossible to find the actual stress state of a hyperstatic masonry structure. In order to analyze a masonry structure with infinitely many stress state solutions, Heyman (1999) describes the master safe theorem of plasticity. This theorem states that if any one equilibrium state can be found for the structure under given loads where the thrust line is contained wholly within the material, then the structure is safe.

An equilibrium state is one that satisfies two conditions: there is a set of internal forces which is in equilibrium with the external forces, and the loads induce compression-only stresses below the yield strength of the material, where the resultant forces are contained within the boundary of the material. Heyman's three assumptions for masonry materials provide a framework for understanding this strength criterion. The first assumption is that the masonry has no tensile strength. While an individual block may have some tensile capacity, the purpose for this conservative assumption is the weak tensile strength of the mortar between the blocks. The second assumption is that the masonry has infinite compressive strength. Because the stresses induced within historic masonry structures made of blocks of stone are typically an order of magnitude lower than the strength capacity of the material, the compressive strength is assumed to be unlimited. The final assumption is that no sliding failure occurs between the masonry (Heyman 1999).

The masonry structure of interest, an arch, carries load axially in compression to the abutments. Because the material is assumed to be infinitely strong in compression, the crushing of the masonry is not the primary concern in masonry analysis. Rather, it is a problem of stability, which is influenced by the geometry of the structure. For a simple two-dimensional analysis, stability is easily understood through the use of the thrust line, the line composed of the consecutive resultant forces acting through each segment of material. This line displays the compressive load path to the supports for the given set of externally applied loads (Block et al.

2006). As mentioned in the safe theorem, a structure is stable when the thrust line is fully contained within the material (Heyman 1999). Instability occurs at the creation of hinges, which form if the thrust line intersects the material boundary. Hinges allow for rotation in one direction and the formation of four or more hinges produces a collapse mechanism, shown in Figure 1-3 (Block et al. 2006).

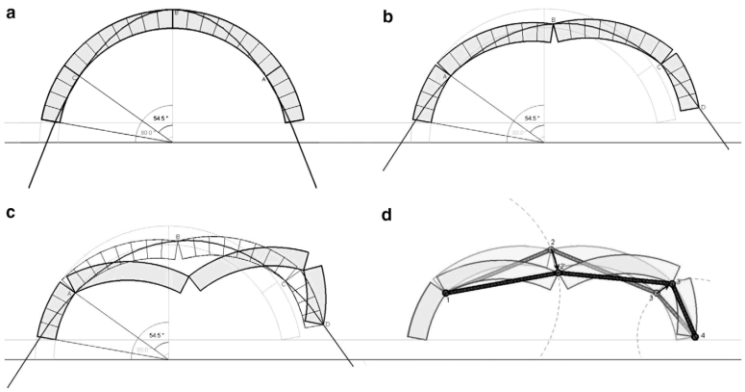

Figure 1-3: Masonry arch on moving supports with (a) stable arch; (b) limit of stability; (c) visualization of mechanism; (d) four bar mechanism (Block et al. 2006)

A geometric factor of safety can be employed to prevent the formation of a collapse mechanism. The thrust line is confined to the inner region of the cross section of the material to prevent the formation of hinges and ensure stability. Heyman (1999) describes a factor of safety of three to avoid tension in the system. This factor of safety, also known as the "middle-third rule" restricts the thrust line to the inner third of the material. The two-dimensional stability analysis of masonry is explored using graphic statics in Chapter 2.

1.2.2 Historic Vaulted Structures

The compressive vault has been a prominent feature of masonry architecture for millennia. A spanning structure in Roman, Medieval, and Renaissance architecture, vaults were traditionally built with brick or stone, but these heavy, bulky structures were structurally inefficient and expensive, due to the weight and cost of material. Later centuries saw a push for shallow vaulted systems that were lightweight enough to reduce the required amount of material needed for the supports, leading to the birth of masonry shell vaults (Bannister 1968).

Although many methods were discovered and adopted by local builders across Europe around the same time, one longstanding style of masonry vaulting was the tile vault. These shallow tile vaults originated in North Africa and grew in popularity in the Mediterranean region,

thanks to the efficient use of material and rapid construction method. Figure 1-4 shows the comparison between traditional stone vaulting and tile vaulting, also known as Guastavino vaulting. The tile vault uses thin tiles, laid flat rather than vertically oriented stone to produce a lightweight vault with less material and a low structural depth. A structure with lower self-weight also yields less thrust and consequently the walls or abutments resisting this force can also decrease in size (Ochsendorf 2010).

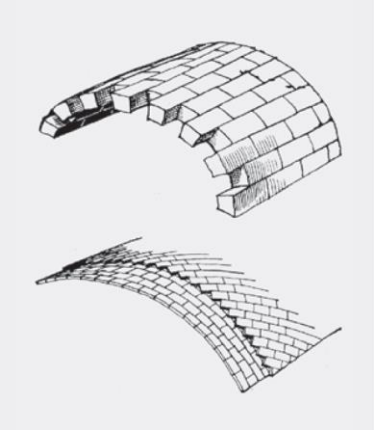

Figure 1-4: Stone (top) versus tile (bottom) vaulting (Moya 1947, reproduced in Ochsendorf 2010)

In addition to the more efficient use of material, tile vaults were advantageous to build due to the simple, rapid construction method. Figure 1-5 shows the construction of three types of masonry vaults. European stone arches were built with wooden centering supporting the stones until the center keystone was set in place. Middle eastern vaults were often pitched so that no centering was required, but this technique required that the vaults have a large rise to span ratio. Tile vaults, however, required neither wooden centering, nor a high rise for construction. Tile vaults were built by successively cantilevering tiles off each other, starting at the supports and working inward until the full arch was built. Fast-setting mortar held the cantilevered tiles in place during construction. Secondary or sometimes tertiary layers of tile were added after the completion of the vault, to provided additional structural thickness (Ochsendorf 2010).

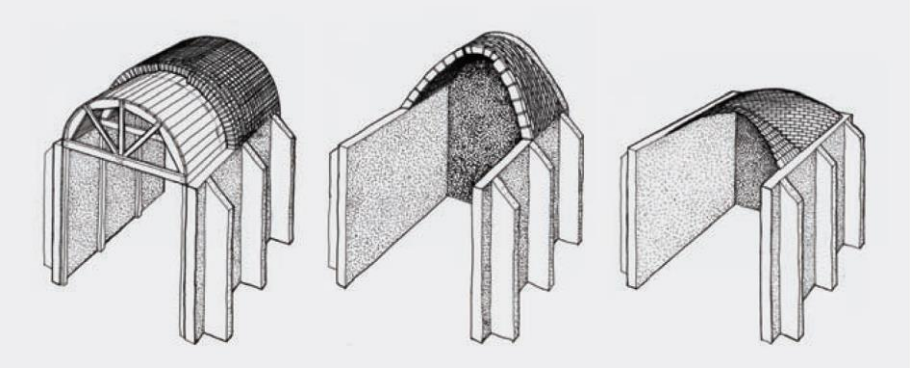

Figure 1-5: Construction of European (left), Middle Eastern (middle), and tile (right) vaults (Drawn by Edward Allen, reproduced in Ochsendorf 2010)

Spanish architect Rafael Guastavino brought the laminated tile vaulting technique to the United States in the late 1800s. Perhaps best well-known for work on the Boston Public Library and the Cathedral of St. John the Divine, Guastavino and his company built floor systems that typically utilized a rise to span ratio of 1:10 (Guastavino 1892). Guastavino Jr. relied on equilibrium calculations to compute the thrust in the vault to determine required thickness of tile, taking into account the material strength, and the required size of masonry buttresses or wrought iron ties. Without the need for falsework or iron beams – the vaults were often supported only by columns and ties – the doubly-curved shell structures were constructed rapidly (Huerta 2003). Despite efficiency of the construction method, one possible reason for the decline of Guastavino vaulting was the increasing cost of skilled labor in the United States (Ochsendorf 2010).

The jack arch was another popular floor system in the United States in the late 1800s and early 1900s. These arches were made of clay tiles, although these tiles were much deeper than those used by Guastavino and are more akin to modern hollow masonry blocks. Arches spanned between parallel steel beams and fill material was added on top of the arch to create a flat floor surface. Jack arches received their name from the timber "jack" beams, which were used in the construction process; jack beams spanned between the structural steel beams and supported the formwork used to construct the arch. Jack arches were either flat or segmental, like that shown in Figure 1-6. Segmental tiles were typically six to eight inches in depth. The combined depth of the tiles and concrete topping was the same as the beam depth so that the beam was braced along its full length. The thrust was resolved using tie rods, although ties were sometimes removed from interior bays after construction, allowing adjacent bays to thrust against each other. Two clear disadvantages exist for the jack arch. First, since interior bays are stabilized by adjacent

bays, the loss of one arch causes instability for the entire system. Secondly, the standard size and shape of the bays were difficult to implement in spaces with irregular geometries (Stuart 2007).

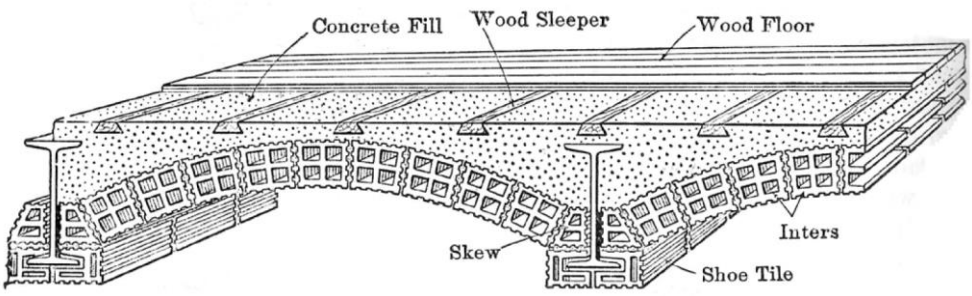

Figure 1-6: Segmental jack arch (Stuart 2007)

1.2.3 Recent Applications of Vaulted Floor Systems

The exploration of thin shell structures is an ongoing area of research today. Swiss engineer Heinz Isler pioneered the use of thin concrete shells for roof structures in the 1950s. One of the most common shell-types built by Isler is the bubble shell, a shallow pillow-like dome, rectangular in plan with a skylight in the center, shown in Figure 1-7. Due to the membrane action of the doubly-curved shell, 90% of the load traveled directly to each corner support and only 10% acted in the edge beams. As a result, the edge beams were slender and only enlarged at the corners to encase the prestressed cable anchorages. Because the frame formed by the shell, edge beams, and columns was quite stiff, the columns also tapered towards the bottom. These shells ranged in sizes from 14 x 20 meters (45.9 x 65.6 feet) to 22 x 22 meters (72.2 x 72.2 ft) and standard size shells were often configured together to create roofs for garages and warehouses with large column-free spans (Chilton et al. 2000). However, Isler did not expand dramatically in the direction of shells for efficient floor systems.

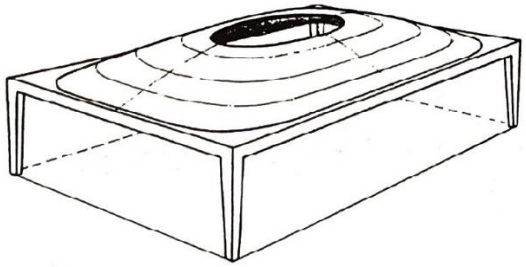

Figure 1-7: Isler bubble shell (Chilton et al. 2000)

The use of thin concrete shells in floor systems was the research focus of William Hawkins (2019) at the University of Cambridge and the University of Bath. Hawkins (2019)

proposed a lightweight, low embodied carbon floor system built from a pre-cast textile reinforced concrete (TRC) shell with lightweight foamed concrete fill, supported at the corners as an alternative to the concrete flat slab. A preliminary study investigated the geometrical design of a 50 mm (2.0 inches) thick shell spanning eight meters (26.2 feet) with a total structural depth of 800 mm (31.5 inches). The parabolic groin vault performed best out of nine different shell geometries, which included mathematically-defined, form-found, and fabric formed shapes. Compared to dome-like geometries, the groin vault has a much lower self-weight since the volume of fill needed on top of the shell is much less (Hawkins et al. 2017). However, the relatively deep rise of 800 mm (31.5 inches) still requires a substantial volume of fill in the groin vault and it would be useful to explore shallower vault geometries.

To cast the TRC shell, timber formwork was assembled from four triangular sections fabricated from 4 mm (0.5 inch) thick sheets of plywood. The sections were bolted together, fixed to a rigid frame, and stiffened with timber sections, shown in Figure 1-8. Hawkins (2019) notes that the construction process was time consuming, but proposes concrete spraying equipment be used to increase the speed of fabrication.

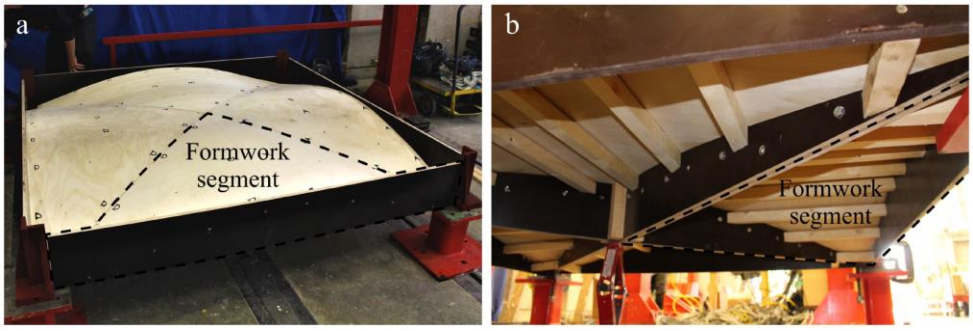

Figure 1-8: Timber formwork for TRC shell (Hawkins 2019)

Hawkins (2019) uses foamed concrete as the fill material, which is only used to transfer applied loads to the TRC shell and provide additional stiffness to the shell. The total self-weight of the shell and fill is 2.53 kN/m^2 (52.8 psf), which is a 65% lighter than the equivalent 300 mm (11.8 inch) thick flat slab under the same loading. The foamed concrete has an ECC of 0.25 kgCO_2e/kg, but this high ECC is balanced by the fact that the density is very low at 50 pcf. Nonetheless, Hawkins (2019) remarks that the fill contributed a great deal more to the total embodied carbon than initially estimated and recommends switching to a low-carbon material.

Technological advances offer new construction methods for optimized vaulted floors. Liew et al. (2017) proposed shallow concrete shells to decrease the structural weight of the floor

system. The system features a shallow compressive concrete vault on the bottom face with rib stiffeners on top (Liew et al. 2017). The shape of the shell is funicular for the dead loads and the rib pattern was determined by force flow. In addition to transferring loads from the floor surface to the vault, the ribs stiffen the entire structure and provide load paths for asymmetrical loads. This principle is illustrated in Figure 1-9: the thrust line under the uniform load fits within the arch material, but a stiffening rib or fill is required to create a viable load path under asymmetrical loads (Block et al. 2017).

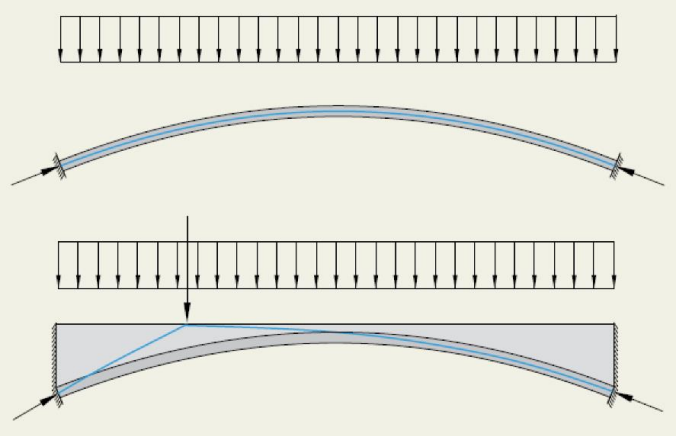

Figure 1-9: Load path through rib under asymmetrical load (Block et al. 2017)

While this floor system is structurally efficient, only using material where necessary to carry loads to the supports, the construction process is intricate and expensive. Figure 1-10 shows the fabrication layers required to cast this rib-stiffened vault, which entail CNC-milled frames and foam blocks. The complex mold needed to create this system makes the structure more challenging to build, through it offers potentially dramatic weight savings.

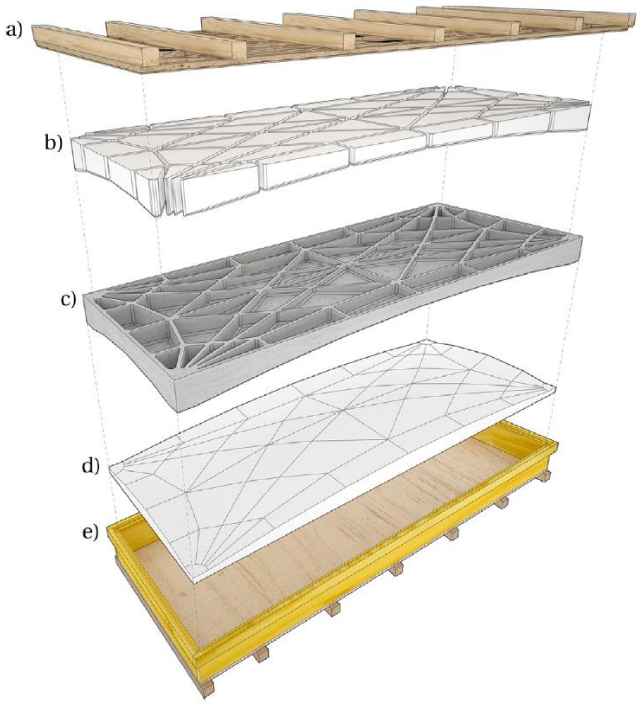

Figure 1-10: Concrete formwork; a) CNC-milled wooden cover frame, b) arrangement of wire-cut foam blocks for the voids and rib formation, c) concrete floor, d) base layer of CNC-milled foam blocks forming doubly-curved vault, e) supporting wooden case (Liew et al. 2017)

Both Wilson (2016) and Gaitan (2021) studied the application of masonry construction with earthen materials for alternative floor systems in developing countries where the cost of steel and concrete is high. Wilson (2016) investigated the structural behavior and design of shallow masonry domes built to produce a design guide for the housing sector in India. Gaitan (2021) further explored the span limits for barrel vaulted floors using unfired adobe, compressed earth blocks, and compressed stabilized earthen bricks. Both theses draw upon equilibrium analysis and plastic design theory in combination with local building techniques to design earthen masonry floor systems.

1.2.4 Autoclaved Aerated Concrete

Advancements in mix design over the past hundred years have led to the production of a wide range of lightweight concretes. One such concrete is autoclaved aerated concrete (AAC). This concrete is made with water, cement, fine aggregate, and the expansion agent, powdered aluminum, which results in a final product that is 80% air (PCA 2019). The aluminum powder reacts with calcium hydroxide and water to form hydrogen, creating macroscopic bubbles in the

mix. The “cake” or mix set into molds, is left to rise for 45 minutes before being cut into blocks of various dimensions. The macroscopic bubbles in the concrete give AAC a very low density. Trustone America reports an AAC density of 37 pcf with a compressive strength of 600 psi and an R-value of 15. Figure 1-11 shows AAC cut into blocks and tiles from a previous thesis by Ramage (2006), which explored the use of AAC for structural tile vaulting.

Figure 1-11: AAC blocks and tiles (Ramage 2006)

Commercial applications for AAC are wall and roof structures, but preliminary research has been conducted to study AAC in vaulted construction as well. Ramage (2006) explored the construction of tile vaults with this lightweight material to investigate the limitations and new possibilities for configurations of masonry structures. Drawing upon techniques of Guastavino vaulting, Ramage (2006) and Lau (2006) constructed a 7-foot diameter shallow dome with AAC tile, using USG Hydrocal as mortar, shown in Figure 1-12. Load applied to the 1.25-inch-thick dome over a 24 inch diameter circle reached 900 pounds before the dome yielded. The structure was very stiff and deflected less than 0.05 inches prior to yielding. The failure characteristics of the structure matched those of typical masonry, suggesting that AAC can be used in structural masonry applications. Ramage (2006) also tested the tensile strength of tiles bonded with Hydrocal to confirm that the tensile capacity of the bond to the tile was sufficient to carry the weight of a cantilevered tile during construction. Further tests on AAC material properties and investigation of the behavior of AAC domes were conducted by Lau (2006) in a study on the equilibrium analysis of masonry domes.

Figure 1-12: AAC dome load test (Ramage 2006, Lau 2006)

In addition to the dome, Ramage (2006) also built non-structural tile vaults, noting in particular the versatility of the material. The AAC can be cut with traditional woodworking tools to create tiles shapes to fit complex geometries. Further, an advantage of the lightweight material is the possibility of using large tile sizes. Ramage (2006) estimated a 77% time saving in dome construction when using 16 x 8 x 2 inch tiles, made possible through the lightweight AAC, rather than standard 12 x 6 x 1 inch tiles (Ramage 2006).

In a third MIT thesis by Dessi-Olive (2018), *La Volta Porosa* further demonstrated the verticality of AAC for vaulting. This doubly-curved structure was built with 100 x 200 x 35 mm (3.9 x 7.9 x 1.4 inch) AAC tiles and spanned 4 meters (13.1 feet) at the widest point. Spline formwork consisted of a steel rebar section, which provided load-bearing support at the center of the arch, and a fiberglass rod section, which served as a geometrical guide. This flexible formwork system revealed that complex geometries are achievable with AAC tiles without the need for heavy supports or intricate guides (Dessi-Olive 2018).

1.3 Problem Statement

The goal of this thesis is to propose and study the feasibility of a vaulted floor system as a lightweight, low embodied carbon alternative to a typical flat slab. The proposed design varies from other recent vaulted floor designs as it does not require expensive formwork, complex falsework, or time-consuming construction sequences. Through the use of traditional masonry construction techniques, a tile vault made from lightweight autoclaved aerated concrete (AAC) is built without the use of falsework and designed for the AAC vault to serve as permanent formwork for the poured concrete fill and topping slab. The vaulted floor eliminates the underutilized material from the flat slab, thus reducing self-weight and embodied carbon. The objectives of this thesis are to show that:

- A vaulted floor system provides sufficient load paths during the construction and built phases of the structure under symmetrical and asymmetrical loads.
- Material volumes and weights are easily quantifiable.
- Vaulted geometry with lightweight concrete simultaneously optimizes the self-weight and the embodied carbon of the system.
- AAC is a viable material for the rapid construction of the vault without falsework.

This thesis focuses on structural analysis in two and three dimensions to study the stability of the system under different load cases in Chapters 2 and 3. Calculations of material quantities in these chapters inform the optimization of weight and embodied carbon in Chapter 4, which also considers alternative geometries and fill materials. Experimental testing of AAC with commercially available mortars demonstrates potential for vaulted construction without falsework in Chapter 5. Each section contributes to the design of a lightweight, low embodied carbon alternative for flat slabs.

Chapter 2 : Two-Dimensional Structural Analysis

The proposed geometry for the vaulted floor system is a groin vault. This shape, formed by intersecting barrel vaults, requires minimal fill material and the singly-curved sections are easily approximated with flat, rectangular tiles (Hawkins et al. 2017). The vault can be tied and supported at each corner with steel ties and columns, as shown in Figure 2-1.

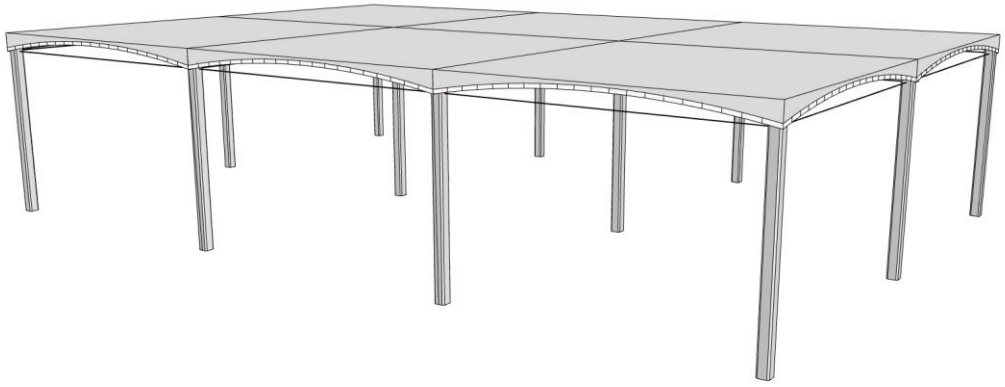

Figure 2-1: Multiple bays of proposed groin vault floor

2.1 Geometry

The geometry of the vault was influenced by recent research on concrete shells and the tile vaults of the 19th century. Out of nine shell geometries proposed by Hawkins et al. (2017), the parabolic groin vault proved lowest in self-weight; thus, a parabolic groin vault is proposed. Equation 2.1 defines the curve of the vault, where *d* is the rise and *L* is the span.

$$f(x) = -\frac{4d}{L^2}x^2 + d \qquad \text{Eq. 2.1}$$

Traditional vaulted masonry floor systems such as those built by Guastavino utilized a rise to span ratio of 10% (Guastavino 1893). Similarly, the parabolic geometry studied by Hawkins et al. (2017) used a 9% rise, where the span is 8 meters (26.2 feet) and the rise is 730 mm (28.7 inches). This study aims to explore the feasibility of the more extreme geometry of 5% rise, which is closer to the typical depth of *L/20* for concrete slabs. Decreasing the rise to span ratio decreases the structural depth of the system and reduces the amount of fill material required, but increases the horizontal thrust and the internal forces. The stresses within the shallow system are the focus of this 2D study.

Consideration of the global system is important to the determination of the 2D span length. The parabola defined by Equation 2.1 describes the curve on the edge faces of the vault, as shown in Figure 2-2. The groin, which runs diagonally across the vault, is approximated as a parabola as well and has the same rise, *d*, as the edge parabolas. However, the groin parabola has a length of $L\sqrt{2}$, rather than L. Thus, the edge span, L, should not exceed 30 feet, else the groin parabola becomes too shallow to be feasibly constructed. The initial chosen geometry for the groin vault is a 20 foot by 20 foot square bay with a one foot rise. The thickness of the AAC tile is set to be two inches. This is the smallest recommended thickness, based on the brittleness of the material and the limitations on cutting the tiles (Ramage 2006). Normal weight concrete is used for the fill and two-inch-thick topping slab.

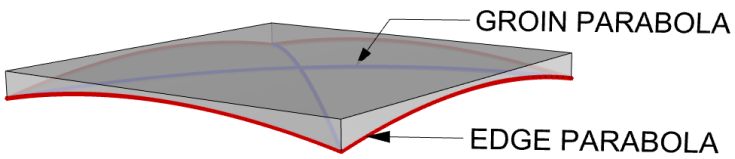

Figure 2-2: Edge and groin parabolas of global system

2.2 Parametric Model

The 2D structural analysis examines a one-foot-wide strip of a parabolic vault, shown in Figure 2-3, which is representative of a load path along the edge parabola. This slice is the foundational geometry of the proposed groin vault system. The strip includes two-inch-thick AAC tile, concrete fill, and a two-inch-thick topping slab, supported by theoretical pins at either end to resist the thrust and vertical loads.

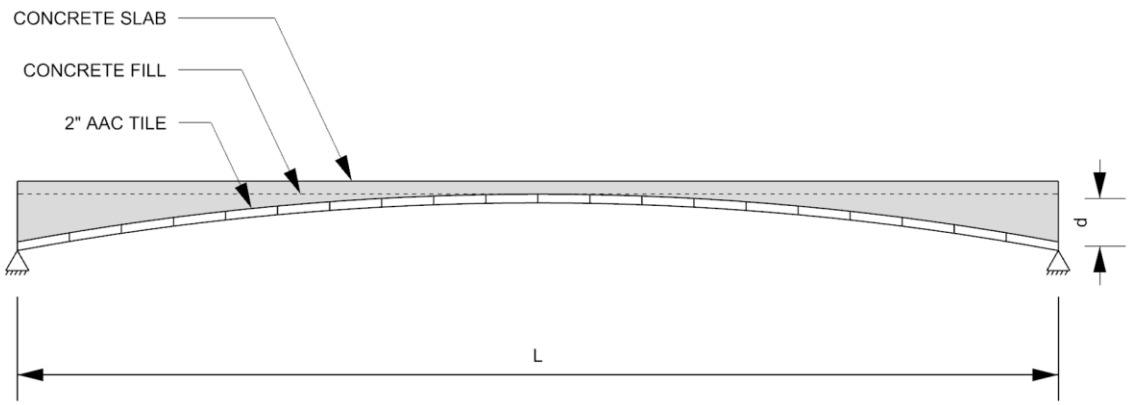

Figure 2-3: Parabolic vault for 2D analysis

The 2D structural analysis considers construction loads and built loads on the vault to determine the lowest possible thrust in the system and ensure that under both conditions the safety criteria for masonry structures set out by Heyman (1999) are satisfied. Stresses within the material and possible load paths are studied to ensure stability within the 2D system.

2.2.1 Thrust Line Analysis with Graphic Statics

Thrust line analysis is an effective tool used to visualize possible load paths through compression only structures (Block et al. 2008). In this study, the equilibrium method used to compute the thrust lines through the vault is graphic statics. This graphical method is based on reciprocal diagrams, where the properties of one are relative to the second (Maxwell 1864). Reciprocal form and forces diagrams are drawn using scaled parallel lines, an example of which is shown in Figure 2-4. The load line on the force diagram is drawn based on the magnitudes of the external loads on the form diagram; closing the force diagram polygons based on a pole creates rays, which map to segments of the resulting thrust line under the given loads (Allen et al. 2010)

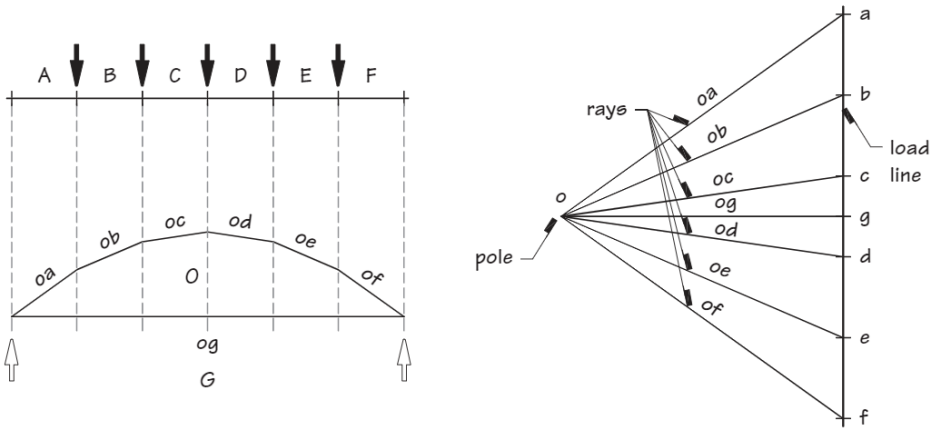

Figure 2-4: Reciprocal form (left) and force (right) diagrams (Allen et al. 2010)

This graphical method is implemented in a parametric model using Grasshopper for Rhinoceros to compute the thrust lines produced in the system under different loads. The Grasshopper script is modified from a script written by Demi Fang, based on a tutorial from InteractiveThrust (Block 2006). The script takes the arch geometry, the centroids of the

discretized arch segments, the end support points, and the magnitude and location of the loads as inputs and provides the force diagram and visualization of the thrust line as outputs.

The model is parametric, so the vault span *L* and rise *d* can be changed to survey different geometries. Further, the pole location of the force diagram is adjusted with sliders and the resulting thrust line updates instantaneously, to provide an interactive exploration of lower bound solutions. Based on a form-found pole location, the resulting thrust line shows one possible path along which load travels to the supports. As noted by Heyman (1999), although infinite solutions are possible, only one of these possible solutions needs to be shown to satisfy equilibrium and lie wholly within the compression-only masonry in order to prove the safety of the structure.

2.2.2 Loads

The vaulted floor system is studied under two separate loading scenarios: construction and built. The construction phase considers the stage where the AAC vault is constructed and acts as formwork for the poured concrete. The load on the AAC is the self-weight of the two-inch-thick AAC and the weight of the wet concrete. The concrete is normal weight concrete, with a density of 150 pcf. The wet concrete has no strength capacity, so the thrust lines in this phase must pass only through the AAC tile. The built phase considers the stage where the concrete has cured and the thrust line passes through the concrete fill. The loads include the same self-weight of the AAC and concrete as in the construction phase, as well as a live load of 100 psf. ASCE-7 prescribes office building live loads of 100 psf for lobbies and first-floor corridors, 50 psf for offices, and 80 psf for corridors above the first floor (ASCE 2013). To be conservative, a live load of 100 psf is applied to the system.

To further study the stability of the system, three load cases are considered for the built phase. The first is a uniform live load, the second is an asymmetrical distributed live load on half of the vault, and the third is an asymmetrical point live load. This point load is applied at the quarter point of the vault and the value is equivalent to the distributed live load on half of the vault distilled into a single point (1 kip). The asymmetrical live loads are studied to ensure that the system has enough structural depth to provide viable load paths for these load cases. Asymmetrical loads are not considered during the construction phase, as the thickness of the AAC is too small to contain the thrust lines from these loads. The intersecting vaults of the AAC vault provide some alternative load path for asymmetrical loads, but quantifying the capacity of

the shallow groin vault under such loading is outside the scope of the current study. The use of ribs or spandrel walls to stiffen shallow tile vaults under asymmetrical loads has been explored, which could be an alternative to provide additional strength during the construction phase (Block et al. 2017). It is specified that loads be applied symmetrically during the construction phase.

Graphic statics requires that the loads on a system are point loads, so the distributed loads discussed above are divided into a series of point loads. The one-foot-wide strip is discretized into one-foot-long segments as shown in Figure 2-5. The loads are applied at the centroid of each segment and the magnitudes are calculated based on the segment self-weight and resultant force from the area load. Note that the concrete fill and slab are monolithic and are not treated as separate loads. Based on the applied loads the vertical reaction *V* and thrust *H* are determined.

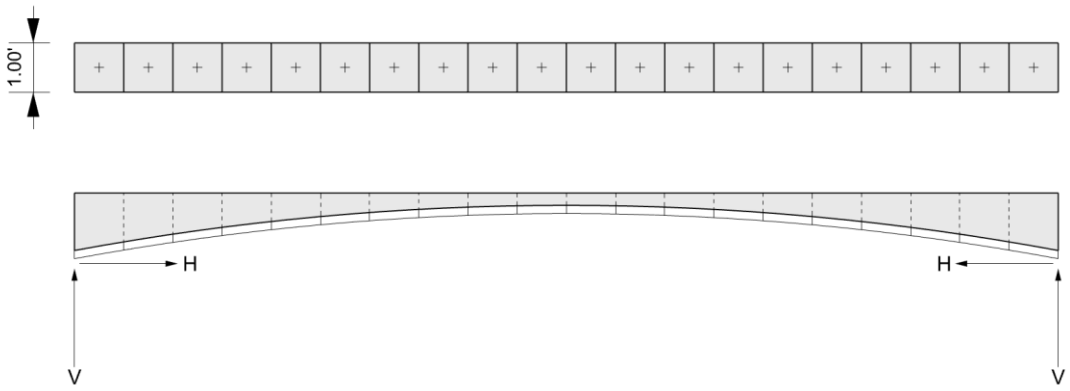

Figure 2-5: One-foot segments of one-foot-wide vault

2.3 Thrust Line Results

The output from the Grasshopper script are the values of the thrust *H*, and the vertical reaction *V*, and the visualization of the thrust line. Additionally, the magnitude of each ray of the force diagram is recorded; from these values, the stress within each one-foot segment is calculated based on uniform stress distribution, using Equation 3-2, where σ is the stress, *F* is the magnitude of the resultant force in the segment, and *A* is the cross-sectional area over which the stress is distributed. The resultant force varies in each section; the maximum force value is used for the calculation of the stress.

$$\sigma = \frac{F}{A} \qquad \text{Eq. 3.2}$$

2.3.1 Construction Phase

Figure 2-6 shows a lower bound solution, minimizing the thrust value in the AAC vault under the tile self-weight and weight of wet concrete. Under these construction loads, the thrust line has been limited to act within the middle two thirds of the vault material as a factor of safety. Since confining the thrust line to the inner two thirds of the two-inch-thick AAC only allows the thrust line to act within a 1.33 inch depth, one inch of mortar topping is advised to be applied to the AAC prior to loading to provide more depth. The mortar has an assumed density of 120 pcf and the mortar weight is added to the total construction load. Figure 2-6 shows the tile vault as three inches thick: two inches of AAC and one inch of mortar. The thrust line fits fully within the middle two thirds, thus displaying a viable, stable load path for these loads.

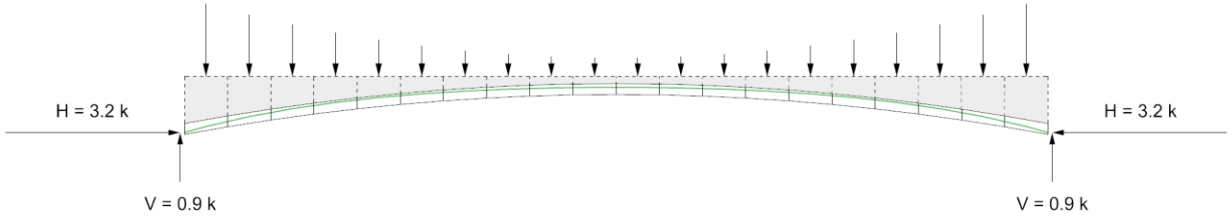

Figure 2-6: Thrust line under construction loads

Under the construction dead loads, the thrust *H* is 3.2 kips and the vertical reaction *V* is 0.9 kips per foot of vault width. The stress distribution used to estimate the maximum compressive stress within the ACC tile is shown in Figure 2-7. The mortar topping does have additional compressive strength, compared to the AAC, but the increased strength capacity of the top one inch of the cross section is conservatively ignored. The cross-sectional area used to compute the stress is a two-inch-deep by 12-inch-wide rectangle; the maximum stress within the tile is 137.5 psi. This stress is well below the compressive strength of the AAC tile, demonstrating the ability of the tile vault to carry the construction loads without any additional support. Postulating a compressive stress zone follows standard convention for strut-and-tie models in reinforced concrete (Beres et al. 2007).

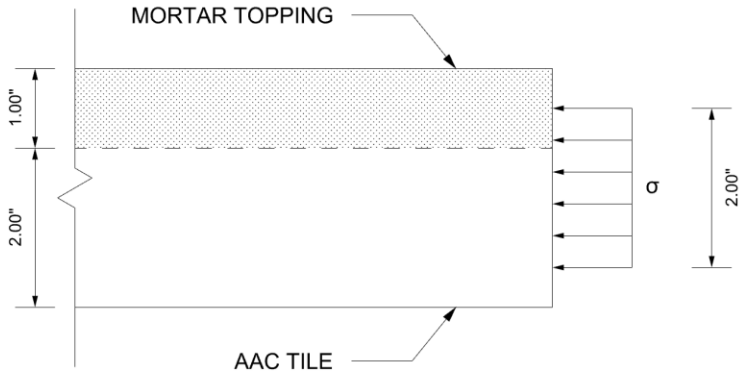

Figure 2-7: Postulated construction phase stress distribution

2.3.2 Built Phase

Figure 2-8 shows a lower bound solution, minimizing the thrust value in the system for the self-weight and applied live loads, where the thrust line is conservatively assumed to act only within the concrete.

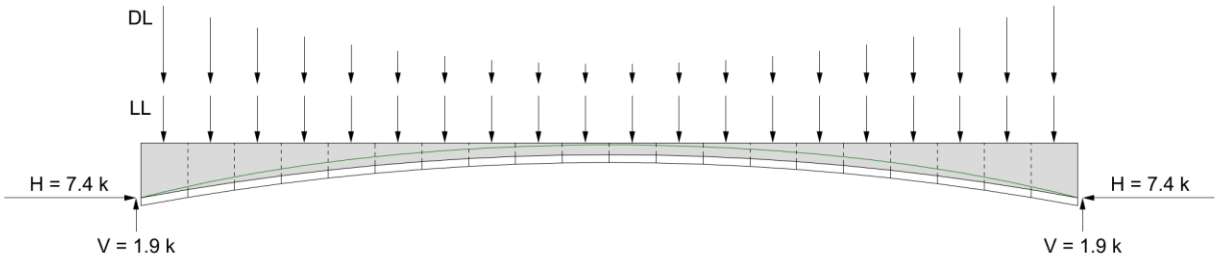

a) Uniform live load

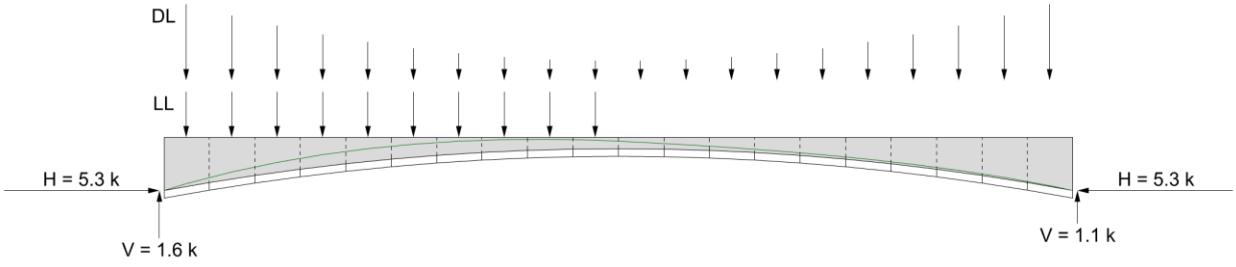

b) Asymmetrical live load

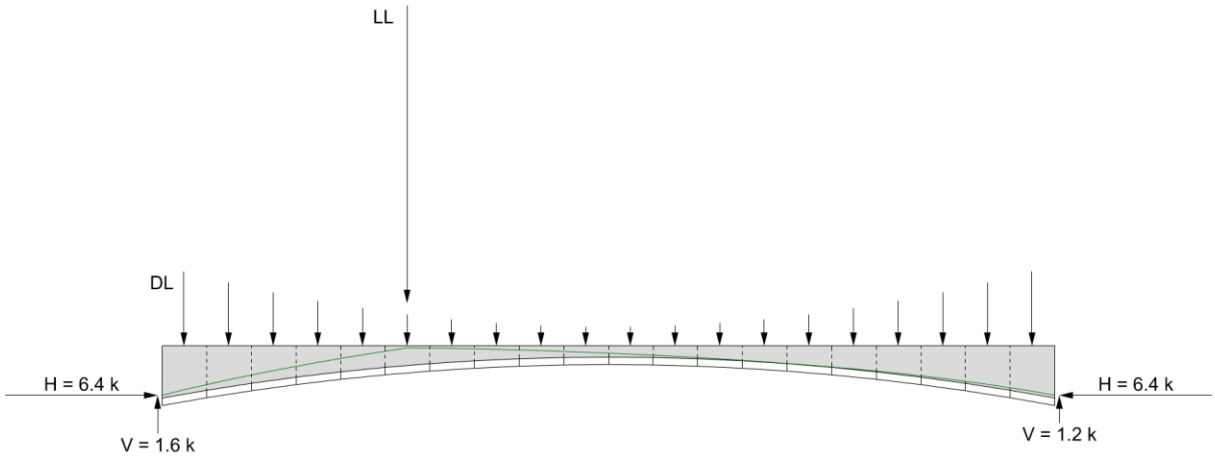

c) Asymmetrical point live load

Figure 2-8: Thrust lines under built loads

The uniform live load case gives the largest thrust value, 7.4 kips, and the largest stress within the concrete, 316 psi because this case has the largest applied load. The stress is calculated based on the cross-sectional area of the most critical segment of the vault; this critical segment is that at the crown, as the segment has the smallest cross-sectional area of concrete. The assumed rectangular stress block for this critical segment is two inches deep by 12 inches wide, shown in Figure 2-9. The stresses induced within the concrete are much lower than the compressive strength of normal-weight concrete, so there is no concern about crushing.

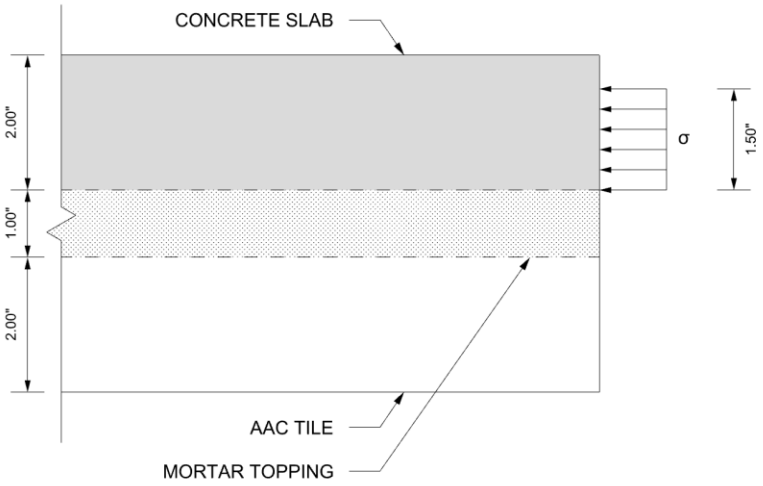

Figure 2-9: Built phase stress distribution

In built phase, the thrust line is assumed to act only within the concrete; the thrust line does not pass through the AAC tile at any point. As an additional factor of safety, the thrust line

also does not act within the top half inch of concrete. While neither of the asymmetrical live load cases induces critical thrust or stress values, it is important to demonstrate that there exist viable load paths under these load scenarios. Figures 2-8b and 2-8c show that these viable load paths exist within the prescribed geometrical factures of safety.

2.4 Alternative Load Paths

The previous sections analyze one-foot-wide slices of the edge parabola, to study load paths along the curve of each individual barrel vault. Within the greater context of the global system, a conservative approach would say that all of the load travels along the barrel, to the groin and then to the supports. Because this is a highly indeterminate problem, it is impossible to know the exact path the load takes. However, a more realistic assumption says that load at the edges take more direct load paths to the support, while load at the crown travels along the groin, similar to the load paths assumed by Wilson (2016). These two load path assumptions are displayed in Figure 2-10. The thrust line along the diagonal is crucial to study since the groin parabola has a smaller rise to span ratio than the edge parabola. This means that internal stresses are higher and viable load paths are more constrained. To verify that possible load paths along the groin parabola exist, the parametric model is modified to model the arch with a $20\sqrt{2}$ foot span and one foot rise. Figure 2-11 shows the tributary area, shaded in gray, for the groin parabola. As previously stated, it is assumed that the load outside of this area takes a more direct path to the support. The load is acting over a 1-foot-wide strip, which is hatched in Figure 2-11.

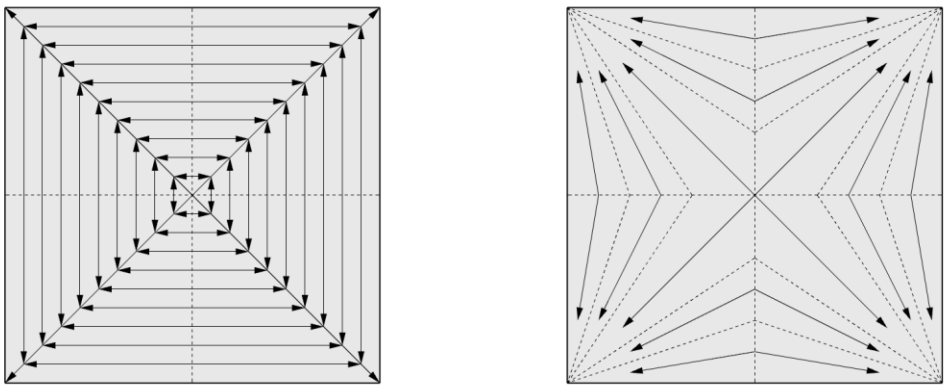

Figure 2-10: Load paths with (left) all load on groin and (right) direct path to the supports

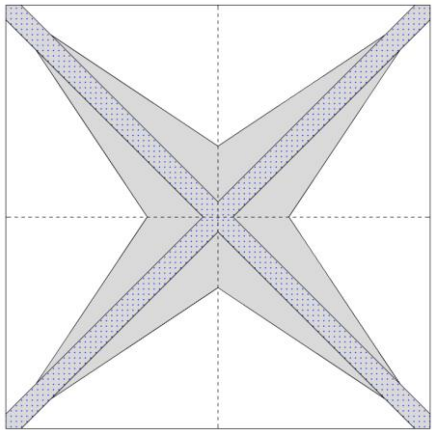

Figure 2-11: Tributary area and 1-foot-wide strip for groin parabola

The thrust line through the AAC from the vault self-weight and wet concrete weight is shown in Figure 2-12. The stress under these construction loads is calculated using the 12 inch by two inch cross-sectional area from Figure 2-7.

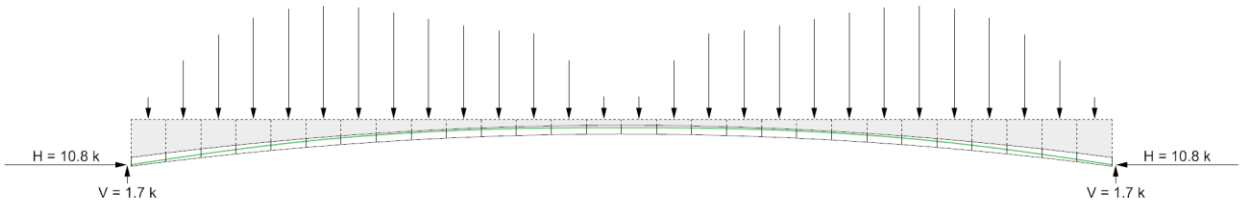

Figure 2-12: Thrust line through groin parabola under construction loads

The maximum stress under the construction loads is 457 psi. This stress is below the AAC ultimate strength so the tile is not susceptible to crushing under this loading. However, the stress in the tile at the corner supports is likely to be much greater than this 457 psi value, as the stresses from other load paths will be concentrated at this point. For this reason, it is recommended that additional masonry mortar be added to the corner prior to pouring the wet concrete, so that the compressive strength in this region will be higher than the AAC compressive strength and the cross-sectional area for the stress to act over will be greater.

Figure 2-13 shows the thrust line in the one-foot-wide groin parabola for the built condition; as before, the dead loads come from the self-weight and the live loads are from the 100 psf area load acting over the tributary area of the groin parabola. The area used to calculate the stress is the two-inch by 12-inch block, shown in Figure 2-9.

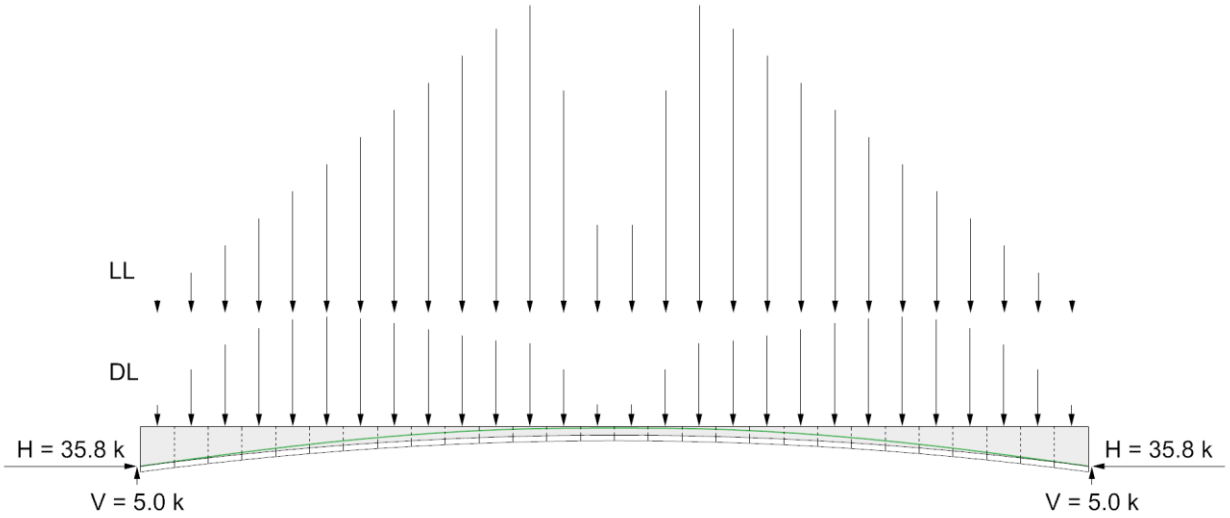

Figure 2-13: Thrust line through groin parabola under symmetrical live load

The maximum stress in the concrete along the vault is 1504 psi. This stress is used to determine the required compressive strength for the concrete fill. Normal-weight concrete, which typically has a compressive strength of 3000 – 6000 psi, satisfies the requirement. The one-foot-wide slice along the groin parabola contains feasible load paths and is stable under construction and built loads.

2.5 Discussion

From the analysis of the edge parabola and groin parabola under construction loads, the AAC tile is determined to have sufficient strength to act as a structural material. The stress in the AAC tile in the edge and groin one-foot-wide slices are 137.5 psi and 457 psi respectively, which are both lower than the 600 psi AAC strength. Under the built loads, the concrete experiences a 316 psi stress in the edge parabola and a 1504 psi stress in the groin parabola, considering the same one-foot-wide area over which the stresses act. These stresses are far below the compressive strength of concrete. Thus, the vault satisfies the strength criterion under construction and built loads. Masonry mortar applied at the corners prior to pouring the concrete would offer additional strength and a less concentrated distribution of stress for an added measure of safety.

The thrust lines output from the parametric model present a visualization of the compressive load path under the various loading scenarios. Each thrust line is shown to fit within

the vault material with the prescribed geometrical factor of safety for each scenario. Not only does the concrete fill act as a structural material to transfer compression to the supports, but it also stiffens the system, providing a safe load path for asymmetrical live loads.

Structural analysis on a 2D "slice" of the 3D systems allows for the exploration of load paths and allowable stresses, assuming single curvature and one-way action. Although composed of singly-curved barrel vaults, the groin vault is itself considered doubly-curved; the groin vault is the intersection of two perpendicular, singly-curved systems and thus carries load in two directions. Since the slicing techniques is only able to capture load paths given one degree of curvature, the results determined in the 2D analysis are conservative, as the double curvature of the system and additional load paths in 3D are not considered. The next chapter considers structural analysis of the system in three dimensions and provides a comparison between the 3D solution and the 2D thrust calculations.

Chapter 3 : Three-Dimensional Structural Analysis

This chapter focuses on calculations of material quantities for the global system. The calculations of the weight and embodied carbon for the 20 foot by 20 foot groin vault geometry shown in this chapter also inform the optimization of the system in Chapter 4.

3.1 Global Resolution of Thrust

The intention of this study is for the 20 foot by 20 foot square groin vault to serve as module of a larger system. Each groin vault produces its own thrust at the corners, but when these bays are built back to bay, there are multiple solutions for resolving the thrust in the global system. Figure 3-1 from Hawkins (2019) shows how buttressing or ties can resolve the global thrust in different ways.

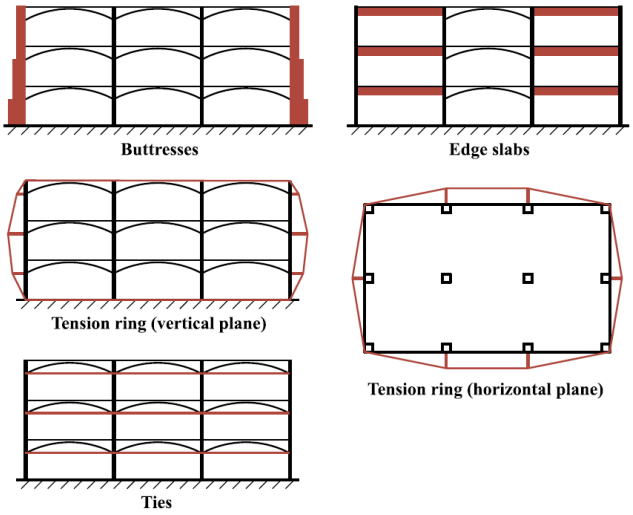

Figure 3-1: Resolution of thrust (Hawkins 2019)

While some systems allow for adjacent bays to thrust against each other and simply resolve the thrust at the perimeter, similar to the jack arch, these systems are not self-stabilized until the full system is built. Resolving the thrust within each bay means that each bay is self-stabilized and that losing a single bay does not affect the stability over the overall system. For the purpose of this study, tension ties around the perimeter of each bay will be used to resolve the thrust so that each bay can act as an individual, stable module. The question of fire protection arises when structural steel is left exposed; the steel ties will need to be protected to achieve safe

fire ratings to satisfy building codes. Methods for mitigating potential risk remain a subject for future work.

3.2 Concrete and AAC Weight

To calculate the total volume of concrete fill in the within the *L* by *L* square groin vault with rise *d*, Equation 3.1 is evaluated. This expression determines the volume between the top of the AAC vault and the bottom of the topping slab for one quarter of the system, shown in Figure 3-2. The fill volume from Equation 3.1 is multiplied by four to find the fill volume for the full vault, shown in Equation 3.2.

$$V_{fill,quarter} = \frac{dL^2}{4} - \int_0^{\frac{L}{2}} \int_{-y}^{y} \left(-\frac{4d}{L^2}x^2 + d\right) dx\, dy = \frac{dL^2}{24} \quad \text{Eq. 3.1}$$

$$V_{fill} = (4)\frac{dL^2}{24} = \frac{dL^2}{6} \quad \text{Eq 3.2}$$

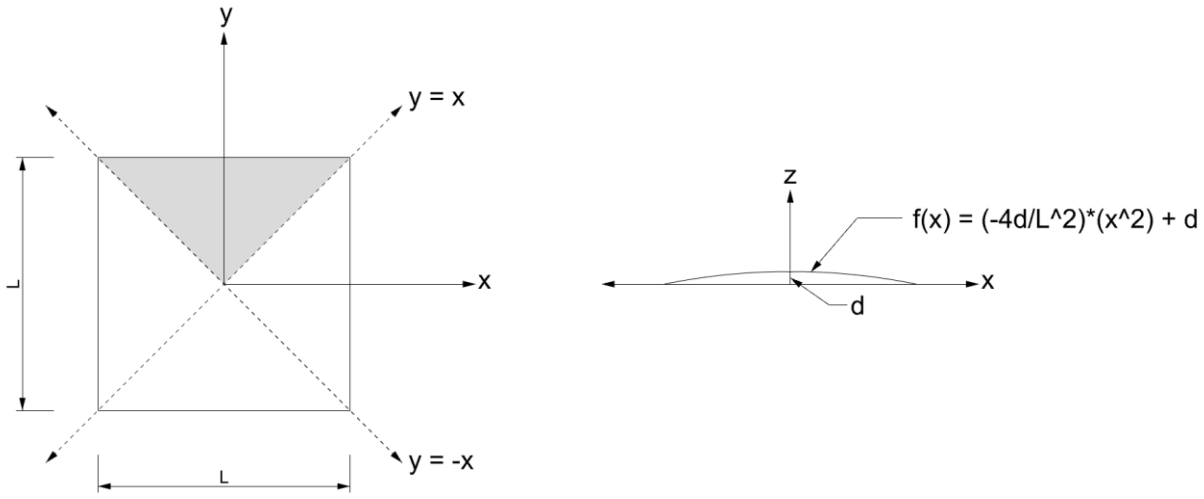

Figure 3-2: Integration bounds for volume of fill

For *L* = 20 feet and *d* = 1 foot, the total volume of fill is 66.7 ft^3; with a density of 150 pcf, the weight of the fill is 10 kips. Similarly, the volume of a topping slab, with t_{slab} = 2 inches, is 66.7 ft^3 with a weight of 10 kips.

Equation 3.3 provides the calculation for the volume of AAC tile, which is also used to compute the volume of topping mortar (Hawkins 2019).

$$V_{shell} = t\left[\left(\frac{L^2}{3} - \frac{L^4}{24d^2}\right)\left(\frac{16d^2}{L^2} + 1\right)^{\frac{1}{2}} + \frac{L^3}{4d}\sinh^{-1}\left(\frac{4d}{L}\right) + \frac{L^4}{24d^2}\right] \quad \text{Eq. 3.3}$$

For t_{AAC} = 2 inches, the volume of AAC is 66.9 ft^3; with a density of 37 pcf, the weight of the AAC is 2.5 kips. The volume of the mortar is 33.4 ft^3 for t_{mortar} = 1 inch; with a density of 120 pcf, the weight of the mortar is 4.0 kips. The total self-weight of the 20 foot by 20 foot groin vault is 26.5 kips.

3.3 Rigid Body Calculation

Rigid body analysis is used to calculate the minimum thrust values at the corner supports of the vault. Externally applied loads and internal stresses are analyzed for one quarter of the full groin vault. The dead load is one quarter of the sum of the weights of the concrete fill, concrete slab, AAC tile and mortar: 6.6 kips. The live load is the uniform 100 psf load applied over the quarter of the vault: 10 kips. The dead and live loads are applied at their respective centroids.

The centroid of the fill for 1/8th of the groin vault, $(\bar{x}, \bar{y}, \bar{z})$ is calculated in Equation 3.4, where $V = dL^2/48$. The quarter groin vault composite centroid, $(\bar{x}_c, \bar{y}_c, \bar{z}_c)$, considers contributions from the fill from two 1/8th sections and the concrete slab, shown in Equation 3.5. The centroid of the concrete slab is ($L/4$, $L/4$, $d + ½\ t_{slab}$). The composite centroid is calculated from the volumes and centroid locations of the concrete slab and fill. For simplification, the volumes of the AAC tile and mortar are not included in this calculation; because the weight of the AAC tile and mortar are small in comparison to the weights of the concrete constituents, they only minorly impact the composite centroid location. Nonetheless, it is assumed that the weight of the AAC tile and mortar act at this composite centroid. The centroid of the live load is located at the point ($L/4$, $L/4$, $d + t_{slab}$).

$$\bar{x} = \frac{\int x dV}{V} = \frac{3}{10}L \quad \text{Eq. 3.4a}$$

$$\bar{y} = \frac{\int y dV}{V} = \frac{2}{5}L \quad \text{Eq. 3.4b}$$

$$\bar{z} = \frac{\int z dV}{V} = \frac{4}{5}d \quad \text{Eq. 3.4c}$$

$$\bar{x_c} = \frac{\sum x_i V_i}{\sum V_i} = \frac{L(7d + 30t_{slab})}{20(d + 6t_{slab})} \quad \text{Eq. 3.5a}$$

$$\bar{y_c} = \frac{\sum y_i V_i}{\sum V_i} = \frac{3L(d + 10t_{slab})}{20(d + 6t_{slab})} \quad \text{Eq 3.5b}$$

$$\bar{z_c} = \frac{\sum z_i V_i}{\sum V_i} = \frac{4d^2 + 30d + 15t_{slab}}{5d + 30t_{slab}} \quad \text{Eq. 3.5c}$$

For L = 20 feet, d = 1 foot, and t_{slab} = 2 inches, the composite centroid is (6 ft, 4 ft, 3.65 ft) and the live load centroid is (5 ft, 5 ft, 1.2 ft). These points of application for the dead and live loads are shown in Figure 3-3. The quarter vault is shown in Figure 3-4. The pin support at the corner resists the vertical load and the thrust in both the x and y directions. The dead and live loads are applied at their respective centroids and the internal stresses on each cut face act over an area of 120 inches by two inches. This 240 in^2 area is the cross-sectional area, *A*, of the concrete at the cut locations. The vertical rise to the centerline of the stress block is 15 inches. *H1* and *H2* are the resultant forces of the internal stresses on the cut faces of vaults; these resultant forces are equal because of the symmetry of the system and symmetrically applied loads.

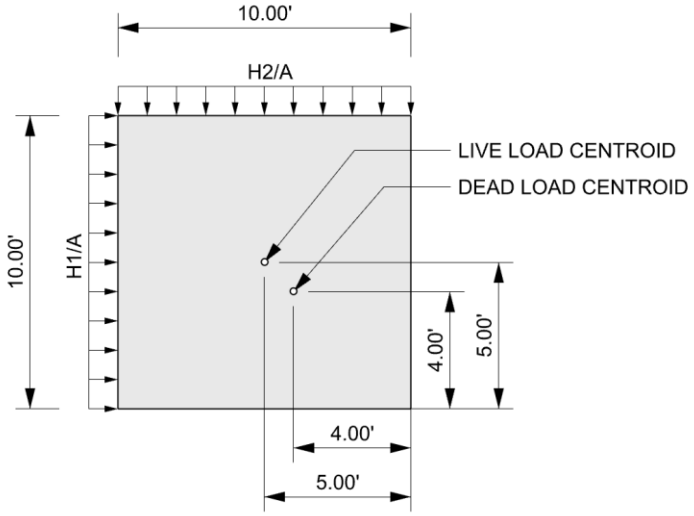

Figure 3-3: Dead and live load centroids on quarter vault

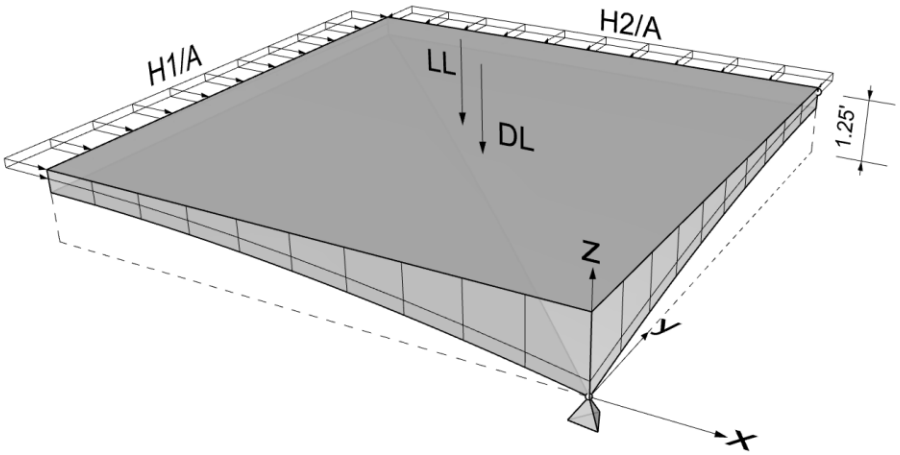

Figure 3-4: Quarter groin vault

In rigid body analysis, equilibrium equations are used to solve for unknown reactions, to ensure translational and rotational stability of the system. Moment equilibria about the x and y axes are used to solve for *H1* and *H2*, which are found to be 61.1 kips for the assumed geometry and loading. These equations confirm that *H1* must be equal to *H2*, based on the symmetry of the system. From translational equilibrium, the pin reaction in the x direction is equal to *H1* and the pin reaction in the y direction is equal to *H2*. Thus, these forces provide the thrust values of the vault at the corners.

To calculate the quantity of steel required for the ties to resist the thrust, Equation 3.6 is used, where σ_s is the allowable stress of steel, assumed here to be 20 ksi, and A_s is the required steel area.

$$A_s = \frac{H}{\sigma_s} \qquad \text{Eq. 3.6}$$

The 20 foot by 20 foot system requires four perimeter ties, each with a cross-sectional area of 3.1 in^2. The process laid out in this chapter for the calculation of material quantities is repeated in Chapter 4 in the comparison of different systems using varied fill material and geometries.

3.4 Discussion

The rigid body calculation offers a method for calculating the thrust at the corner of the groin vault in the longitudinal (x) and transverse (y) directions. This 3D analysis takes into

consideration the two-way action of the groin vault, a factor that was not incorporated into the 2D analysis in Chapter 2. To compare the results from these two methods, the 2D analysis must be converted to a 3D system. Consider an extrusion of the one-foot-wide vault from Figure 2-8a to create a 20 foot by 20 foot barrel vault with one foot rise at the midspan. The thrust in this barrel vault under the uniform 100 psf live load is compared to the thrust in the groin vault under the same live load to compare the two methods.

The 2D analysis found that the thrust of the vault spanning 20 feet is 7.4 kips per one foot strip width. Therefore, the thrust in the 20-foot-wide vault is 7.4 kips multiplied by 20 feet, or 148 kips in the longitudinal direction. From the rigid body analysis, the thrust in the longitudinal direction at one corner of the groin vault is 61.1 kips, so the total longitudinal thrust is 122.2 kips. Thus, the rigid body analysis of the groin vault offers a 17% decrease in thrust and therefore a 17% decrease in steel tie volume from the one-way action of the barrel vault from the 2D analysis. Forces in the transverse direction in the two systems are more difficult to compare: the barrel vault produces a vertical line load which is resisted by a beam in flexure and the groin vault has a transverse thrust which is resisted by an additional tension tie. The comparison of the two systems is further evaluated in Chapter 4 by quantifying the weight and embodied carbon each system.

Chapter 4 : Optimized System

A square groin vault with normal weight concrete is the focus of the 2D and 3D structural analyses previously described. Here, the weight and embodied carbon of different systems that vary in geometry and material usage are explored in order to optimize this system.

4.1 Varied Geometry

The primary goal of this thesis is to design a floor system with a lower weight and embodied carbon compared to a typical flat slab. A one-way 20-foot-wide flat slab, spanning 20 feet, sized for 100 psf live load, is 12 inches thick with 7.0 in^2 of reinforcing steel (sized by Stephanie Baez). A vaulted system of the same depth serves as an alternative floor system which eliminates much of the underutilized material in a flat slab. Although the focus thus far has been on the square groin vault, the natural progression of the design introduces two related systems that ought to be studied as well. These systems are the barrel vault and the rectangular groin vault.

4.1.1 Barrel Vault

The barrel vault, briefly described in the previous chapter, is the simplest expansion of the 2D analysis into 3D. An extrusion of the one-foot-wide edge parabola from Chapter 2 produces a singly-curved barrel vault, which as a result is assumed to carry load only in one direction. The barrel vault, shown in Figure 4-1 is supported continuously on two sides. Therefore, in addition to steel ties to resist the thrust, the proposed barrel vault also utilizes steel perimeter beams to support the vertical load continuously in the transverse direction.

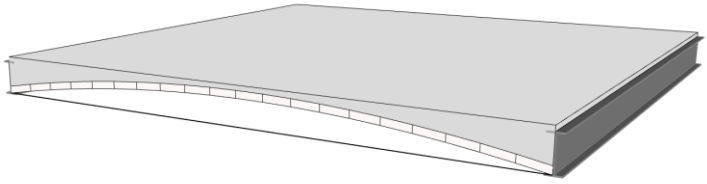

Figure 4-1: Barrel vault with perimeter beams

The volume of fill of an L by L parabolic barrel vault with rise d is shown in Equation 4.1; this value is two times the volume of fill of a square groin vault of the same dimensions.

$$V_{barrel\ fill} = L\int_{-\frac{L}{2}}^{\frac{L}{2}} \frac{4d}{L^2}x^2 dx = \frac{dL^2}{3} \quad \text{Eq. 4.1}$$

As the vault is nearly flat, the AAC tile and mortar volumes are calculated by multiplying their thicknesses by the floor area, L^2. Considering two-inch-thick AAC tile, one-inch-thick mortar topping and two-inch-thick topping slab along with the fill material, the self-weight of a 20 foot by 20 foot barrel vault with a midspan rise of one foot, excluding the weight of steel, is 36.5 kips. As shown in Figure 2-8a, the vault in 2D under 100 psf live load has a vertical reaction of 1.9 kips and a thrust of 7.4 kips. Extruding this one-foot-wide slice into a 20-foot-wide system produces a vertical reaction of 1.9 kip/ft and longitudinal thrust of 7.4 kip/ft. The thrust is resolved with steel tension ties, as in the case of the groin vault. Using Equation 3.6, the required area of steel is 7.4 in^2. However, unlike the groin vault, which is supported only at the corners, the vertical reactions on this one-way system produce a line load, which loads a perimeter beam in bending on either side of the vault. Using Table 3-10 from AISC Steel Construction Manual, a beam sized for a load of 3.8 kip/ft, assuming the beam carries load from two adjacent bays, is W16x31; the atypical loading of the beam illustrated in Figure 4-1 is ignored in this scenario (AISC 2017). The perimeter beam needed to support the singly-curved barrel vault adds additional weight and embodied carbon to the system.

4.1.2 Rectangular Groin Vault

The other alternative system to consider is the rectangular groin vault: rather than an *L* by *L* bay, here an *L* by *1.5L* bay is considered. One clear advantage of this elongated system is the ratio of floor area to number of columns. For example, an area of 1200 ft^2 would require eight columns using 20 foot by 20 foot square system, but only six columns if the bays were 20 foot by 30 foot. Eliminating columns and spanning long distances with the vault provides a more flexible use of the space. The stresses in this system were not verified in the 2D analysis, but the rectangular groin vault is still a potential optimal solution.

Equations 3.1 and 3.2 are modified to calculate the volume of fill in an *L* by *1.5L* groin vault: $dL^2/4$. Interestingly, the normalized fill volume – the volume of fill divided by the bay area – is equivalent for the square and rectangular groin vault. As the vault is nearly flat, the surface

area of AAC tile and mortar are simply scaled by a factor of 1.5, keeping the same thicknesses as before. The total dead weight of a 20 foot by 30 foot groin vault with a midspan rise of one foot is 39.7 kips. The rigid body calculations from Chapter 3 are replicated for this rectangular system to calculate H1 and H2, which are 137.7 kips and 91.8 kips, respectively. Therefore, using Equation 3.6, the required steel area for ties in the x and y directions are 6.9 in^2 and 4.6 in^2, respectively.

4.1.3 Column Sizing

The proposed floor system is designed to serve as one bay of the total floor area, where multiple bays can be constructed adjacent to one another. Much like Isler's bubble shells, four vaults can be assembled with only one interior column (Chilton et al. 2000). Corner columns are sized for this scenario, where each column carries the load from one quarter of each the neighboring bays. This column tributary area is shown in Figure 4-2; the square systems –the flat slab, barrel vault and square groin vault – have tributary areas of 400 ft^2 and the rectangular groin system has a tributary area of 600 ft^2. The columns sizes for each of the four systems under 100 psf live load with a 12-foot effective length are shown in Table 4-1, based on Table 4-3 from the AISC Steel Construction Manual (AISC 2017).

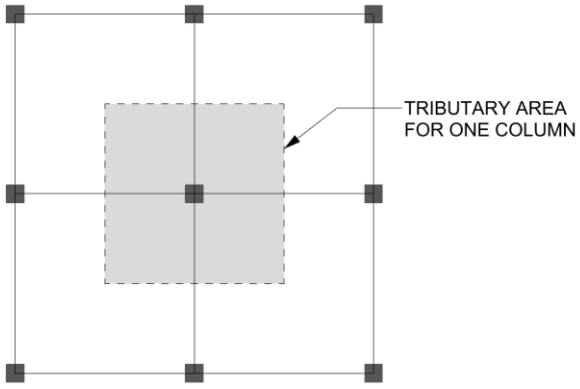

Figure 4-2: Column tributary area

Table 4-1: Column Sizes for each system (prepared by Stephanie Baez)

	Column Trib Area (ft^2)	Dead Load (k)	Live Load (k)	Column Size	Column Capacity (k)
Flat Slab	400	60.0	40.0	HSS 6 x 5 x ¼	138
Barrel Vault	400	37.1	40.0	HSS 7 x 4 x ¼	118
Square Groin Vault	400	26.5	40.0	HSS 6 x 5 x 3/16	106
Rectangular Groin Vault	600	39.8	60.0	HSS 5 x 4 x ½	150

4.1.4 Comparison of Weight and Embodied Carbon

The weight and embodied carbon of four systems, the flat slab, the barrel vault, the square groin vault, and the rectangular groin vault, are compared to determine the most optimal system. The embodied carbon is calculated by multiplying the weight of each material by its corresponding embodied carbon coefficient; Table 4-2 lists the embodied carbon coefficients estimated for each material (Jones et al. 2019). Figure 4-3 shows the total weight and embodied carbon of each system, broken down into material components, normalized by the floor area. In addition to the concrete, AAC, and mortar, the steel reinforcement, ties, columns, and, in the case of the barrel vault, beams are all included in the weight and embodied carbon calculations.

Table 4-2: Embodied carbon coefficients (Jones et al. 2019)

Material	Embodied Carbon Coefficient
Normal weight concrete	0.20
AAC	0.28
Mortar	0.20
A992 Steel	1.23

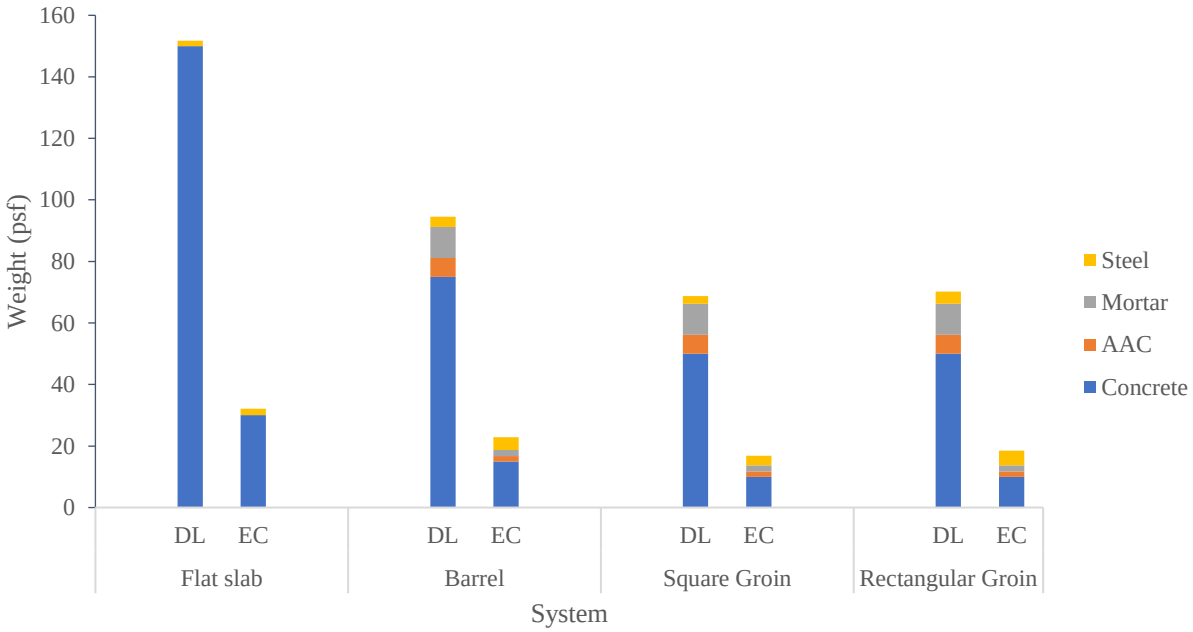

Figure 4-3: Normalized dead load (DL) and embodied carbon (EC) breakdown for different geometries

As seen in the figure, the barrel vault, square groin and rectangular groin vault all show improvements over the flat slab in both the structural weight and embodied carbon. Since the barrel vault has a higher volume of fill than the groins, it exhibits the worst performance out of the three vaulted systems. When normalized by the floor area, the two groin vaults perform almost identically. The rectangular groin, however, presents complications for construction, because of its extremely low rise to span ratio of 1:30 in the long direction, a complication which falls outside the scope of this thesis. The normalized weight and embodied carbon of the square groin vault are 68.7 psf and 16.8 psf, respectively.

4.2 Alternative Concrete Types

The final stage of the design exploration looks at the effects of using alternative concrete mixes for the fill and topping slab of the square groin vault. As shown in the geometry optimization, the concrete is the primary contributor to the structural weight and embodied carbon of the system. Using a concrete of lower density decreases the weight of the system; however, it is not as obvious whether lightweight concrete mixes will decrease the embodied carbon, since the embodied carbon is impacted by both the density and the ECC. Six different

"lightweight" concretes are considered as alternatives to the previously considered normal weight concrete; the properties of the concretes are shown in Table 4-3.

Table 4-3: Concrete properties (prepared by Stephanie Baez)

		Density (pcf)	Compressive Strength (psi)	ECC (lb-CO_2e/lb)	Source
Normal weight concrete		150	4000	0.20	Jones et al. 2019
Foamed concrete		50	140	0.25	Hawkins 2019
Conventional lightweight concrete		90	1700	0.31	Ersan et al. 2020
Concrete with lightweight aggregate	**Recycled plastic + fly ash**	87	1300	0.26	
	Glass bubbles	93	3300	0.19	Yun 2013
	Manufactured LW coarse aggregate	100	3300	0.18	Robati et al. 2016
	Wood waste replacement	100	1200	0.14	Alexandru et al. 2019

4.2.1 Compressive Strength Check

While all the concrete alternatives are lower in density than the normal weight concrete, they range in ECC and compressive strength. The compressive strength is particularly important, as the thrust line under built conditions is fully encapsulated by the fill. Therefore, the material must have enough compressive strength to carry the internal forces induced by the self-weight and live load to the supports without crushing. To determine which concretes are viable alternatives under this strength criterion, the compressive strengths are compared to stress in the fill in the 2D groin parabola. To reiterate, this slice is representative of the most critical load path of the entire system as it has the lowest rise to span ratio, and thus greatest internal forces. The parametric model is updated with the fill densities of each type of concrete and the required strength for each type is shown in Table 4-4. Concretes with a compressive strength lower than the required strength are not considered viable alternatives to normal weight concrete.

Table 4-4: Compressive strength and required strength for concrete

		Density (pcf)	Compressive Strength (psi)	Required Strength (psi)	Viable? (Y/N)
Normal weight concrete		150	4000	1500	Y
Foamed concrete		50	140	1220	N
Conventional lightweight concrete		90	1700	1335	Y
Concrete with lightweight aggregate	**Recycled plastic + fly ash**	87	1300	1325	N
	Glass bubbles	93	3300	1345	Y
	Manufactured LW coarse aggregate	100	3300	1365	Y
	Wood waste replacement	100	1200	1365	N

4.2.2 Material Calculation

The volume of concrete, AAC tile, mortar, and steel are calculated using the same process laid out in Chapter 3. The volume of concrete, AAC, and mortar are the same for all concrete types. As previously mentioned, the *H1* and *H2* reactions are equivalent in a square groin vault due to symmetry. The thrust value, as well as the cross-sectional area of the steel tie needed to resist it, are shown in Table 4-5. The columns were sized based on the tributary area shown in Figure 4-2. The column size for each concrete type with a tributary area of 400 ft^2 is shown in Table 4-6.

Table 4-5: Thrust and steel tie cross-sectional area

		Thrust (k)	Steel Area (in^2)
Normal weight concrete		61.1	3.1
Foamed concrete		50.5	2.5
Conventional lightweight concrete		54.8	2.7
Concrete with lightweight aggregate	**Recycled plastic + fly ash**	54.5	2.7
	Glass bubbles	55.1	2.8
	Manufactured LW coarse aggregate	55.9	2.8
	Wood waste replacement	55.9	2.8

Table 4-6: Column sizes for each concrete type (prepared by Stephanie Baez)

		Dead Load (k)	Live Load (k)	Column Size	Column Capacity (k)
Normal weight concrete		26.5	40.0	HSS 6 x 5 x 3/16	106
Foamed concrete		13.2	40.0	HSS 6 x 3 x 3/8	81.7
Conventional lightweight concrete		18.5	40.0	HSS 5 x 4 x ¼	90.3
Concrete with lightweight aggregate	**Recycled plastic + fly ash**	18.1	40.0	HSS 5 x 4 x ¼	90.3
	Glass bubbles	18.9	40.0	HSS 5 x 4 x ¼	90.3
	Manufactured LW coarse aggregate	19.8	40.0	HSS 6 x 3 x ½	95
	Wood waste replacement	19.8	40.0	HSS 6 x 3 x ½	95

4.2.3 Comparison of Weight and Embodied Carbon

In addition to structural capacity, the performance of each concrete is also measured by the impact on the structural weight and embodied carbon for the overall system. Figure 4-4 displays these quantities, broken down by material and normalized by the floor area, for each type of concrete. Again, the embodied carbon is calculated by multiplying the weight of each material by its corresponding embodied carbon coefficient.

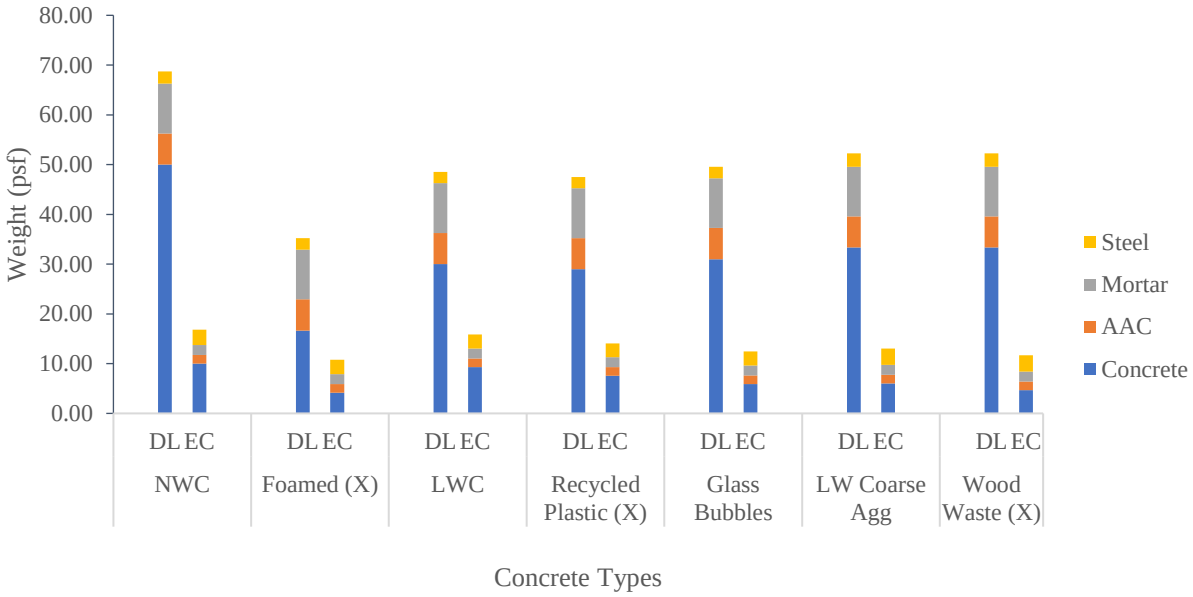

Figure 4-4: Normalized dead load (DL) and embodied carbon (EC) breakdown for different concretes

All the lightweight concretes showed reductions of both the structural weight and embodied carbon over the normal weight concrete, but of the six alternatives, three are not viable options, as they do not meet the strength requirement – these options are marked on Figure 4-4 with an (X). The extremely low density of foamed concrete proposed by Hawkins (2019) balances the high ECC, allowing it to be the system of lowest structural weight and embodied carbon; however, this concrete is one of the three that does not meet the strength requirement for the shallower geometries considered in this thesis. The range of structural weight was quite small for the three remaining viable options; the lightweight concrete with glass bubbles proved to be the most ideal option as it has the lowest embodied carbon. The normalized weight and embodied carbon of the square groin vault with lightweight concrete with glass bubbles are 49.5 psf and 12.5 psf, respectively.

4.3 Discussion

The purpose of this thesis is to design an alternative floor system to the typical flat slab that produces a reduction in weight and embodied carbon through more efficient material use. The 12-inch-thick flat slab with reinforcing steel has a weight of 151.7 psf with 32.1 psf of embodied carbon. This embodied carbon value is confirmed by De Wolf et al. (2016) where the embodied carbon of a two-story building with flat slabs spanning 10 meters (32.8 feet) was 230

kg_{CO2e}/m^2 (47.1 psf). It is important to note that De Wolf et al. (2016) calculate the cradle-to-grave embodied carbon, whereas the current study calculates only the embodied carbon from the materials themselves.

Of the three vaulted systems – the barrel vault, square groin vault, and rectangular groin vault – the groin vault proved to be the optimal alternative geometry to the flat slab. At 68.7 psf for the structural weight and 16.8 psf for the embodied carbon, the square groin vault has a 55% decrease in structural weight and a 48% reduction in embodied carbon. Using a lightweight concrete with glass bubbles rather than normal weight concrete decreases the values further to 49.5 psf of structural weight and 12.5 psf of embodied carbon. This alternative concrete shows a 67% reduction in structural weight and a 61% reduction in embodied carbon compared to the flat slab.

The next chapter will explore the feasibility of commercially available mortars for use with AAC in the construction of tile vaults.

Chapter 5 : Experimental Testing

5.1 Background

AAC, shown in Figure 5-1, is the proposed material for the vaulted formwork of the floor system because it is lightweight (37 lb/ft^3) and easy to cut into appropriately sized tiles. As the literature review discussed, previous theses by Ramage (2006), Lau (2006), and Dessi-Olive (2018) explored the potential for AAC as a vaulting material, but did not systematically explore options for mortar of sufficient strength during the construction of floor systems. This chapter presents new experimental tests to determine the flexural capacity of a mortared AAC joint to simulate performance under construction loads and to test several possible mortars. The four-point flexure test discussed in this chapter provides insight into the maximum tile size that can be cantilevered in the construction of a vault without falsework. Splitting tensile tests are also conducted on each mortar; the results from these tests are presented in the Appendix. All tests were conducted in the Pierce Laboratory at MIT with the support of Stephen Rudolph.

Figure 5-1: 4 x 8 x 24 inch AAC block

In two prior theses focused on the construction and behavior of masonry domes, Ramage (2006) and Lau (2006) performed preliminary experimental tests on AAC, which was provided by Trustone America of Providence, Rhode Island. Both theses tested bonded tile specimens of varying thickness (one, two, and four inches thick) in flexure. Because of the fragility of the tile, Ramage (2006) recommends a minimum thickness for construction applications of two inches, which is the thickness used in the design of the tile vault presented in the current thesis. This

chapter considers two-inch bonded tile specimens using three commercially available mortars to determine the feasibility of AAC as a construction material for vaulting.

The mortars tested in the experiments are USG Hydrocal White Gypsum Cement (USG 2021), CTS Rapid Set Mortar Mix (CTS 2021), and Silpro Thin Deep Quick (TDQ) Repair (Silpro 2021). Each mortar is a cement-based fast-setting mortar mix which need only be mixed with water to prepare for use. Table 5-1 shows the water to dry mix ratio used for each product, informed by the manufacturer recommendations.

Table 5-1: Water to dry mix ratios

Product	**Water to Dry Mix Ratio (by mass)**
USG Hydrocal	0.40
CTS Rapid Set	0.18
Silpro TDQ	0.19

5.2 Four-Point Flexure Test

5.2.1 Methodology

The first test performed is a four-point flexure test, which is used to determine the modulus of rupture (flexural strength) of the specimens. The test is modified from ASTM C67, “Standard Test Methods for Sampling and Testing Brick and Structural Clay Tile” (ASTM, 2020). The test is modified from the standard three-point flexure test so that no load is applied directly at the mortared joint between the tiles. A schematic of the test setup is shown in Figure 5-2, showing the spacing between the supports, and the actual test setup is shown in Figure 5-3.

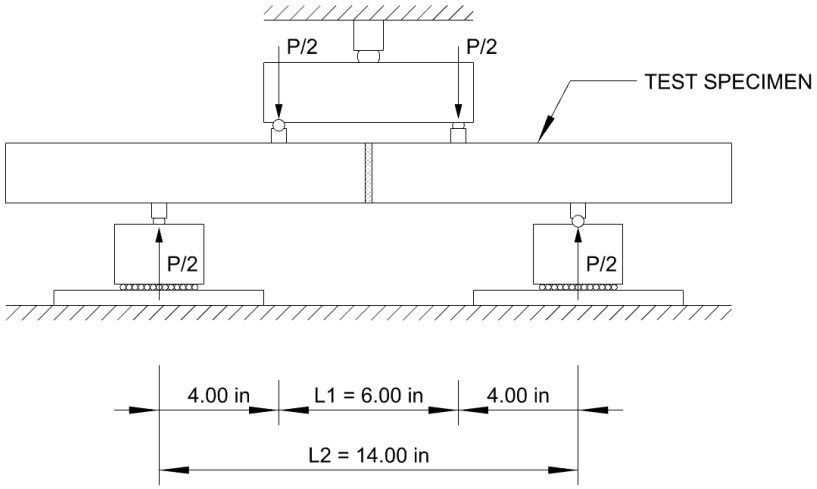

Figure 5-2: Schematic of four-point flexure test setup

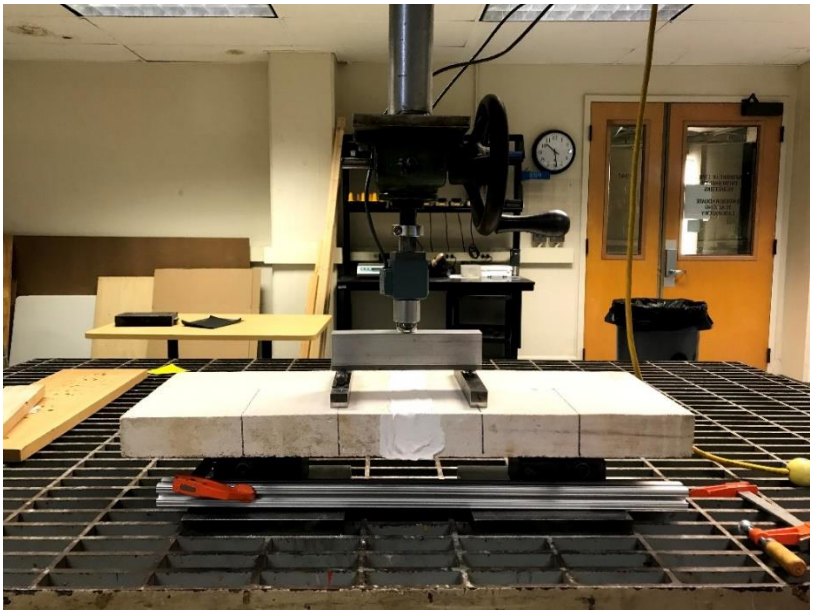

Figure 5-3: Actual four-point flexure test setup

The test is performed on a manual loading machine and the applied force and displacement of the specimen are recorded digitally by a load cell and extensometer. Based on the maximum load P, the flexural strength σ, is calculated using Equation 5.3, where L_1 and L_2 are the distance between the outer and inner supports, respectively, b is the width of the specimen (12 inches), and d is the depth of the specimen (two inches). Based on the maximum moment at the midspan, Equation 5.1, and the stress due to bending, Equation 5.2, the maximum bending stress is defined in Equation 5.3:

$$M = \frac{P}{2}(L_2 - L_1) \quad \text{Eq. 5.1}$$

$$\sigma = \frac{M}{S} = \frac{6M}{bd^2} \quad \text{Eq. 5.2}$$

$$\sigma = \frac{3P(L_2 - L_1)}{2bd^2} \quad \text{Eq. 5.3}$$

The specimens were prepared by first cutting the AAC blocks into the appropriate size. Based on the dimensions of the test set up, the blocks were cut into 12 x 6 x 2 inch tiles using a standard 14-inch band saw with carbide-tipped blade. The tiles were oven-dried at 80˚for 24 hours and stored in a dry place at room temperature.

Mortar was applied to both tiles first, before pressing the two tiles together with joint width of ¼ inch. Spacers were placed between the two tiles and the excess mortar was pressed out from between the two tiles. The specimens were left to set for 48 hours before testing.

Six test specimens, two of each mortar type, were prepared in order to understand the workability and application process of each mortar as a preliminary step. One round of specimens was set by applying the mortar to the dry tile face. The other round of specimens was set by first dipping each tile face in an inch of water for three seconds before applying the mortar. The final tests specimens were set using this "wet-face" mortar bond method, which gave strong cohesion with the porous AAC.

5.2.2 Preliminary Results

The force versus displacement plots for each of the six preliminary test samples are shown in Figure 5-4. The failure point for the dry face specimens all occurred at the interface between the mortar and the tile, while the wet face specimens failed near the bond, but within the tile, shown in Figure 5-5. The wet face specimens achieved a stronger mortar bond to the AAC tile, since the moisture within the mortar was not absorbed by the tile. Pre-moistening the tile prevents the loss of moisture in the mortar that decreases the bond strength. Based on these preliminary results, the final flexural tests were conducted using a wet face bond.

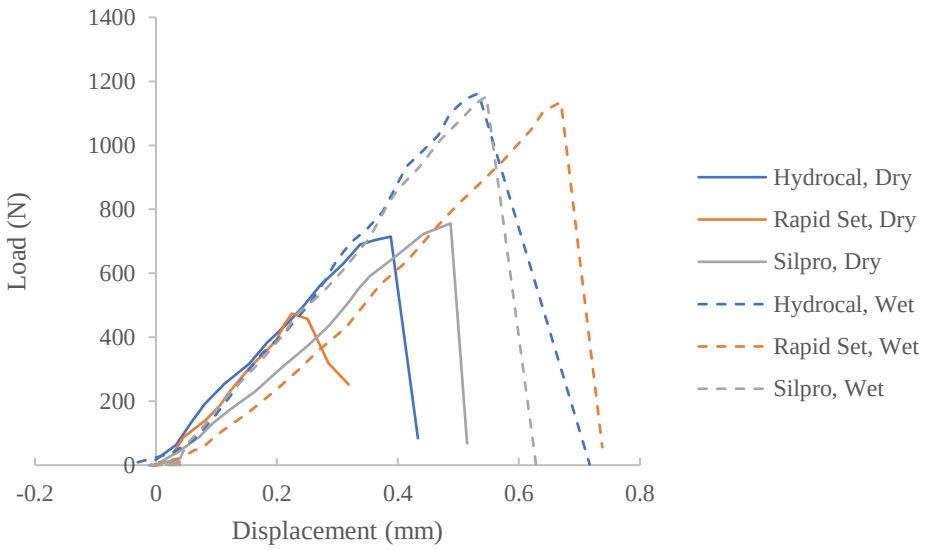

Figure 5-4: Wet face versus dry face bond test

(a) Dry face bond

(b) Wet face bond

Figure 5-5: Post-experiment Silpro TDQ specimens

5.2.3 Final Results

In the final tests, nine specimens were tested, three with each mortar type, in order to have statistically meaningful results. The load versus displacement plots for each mortar type are shown in Figure 5-6.

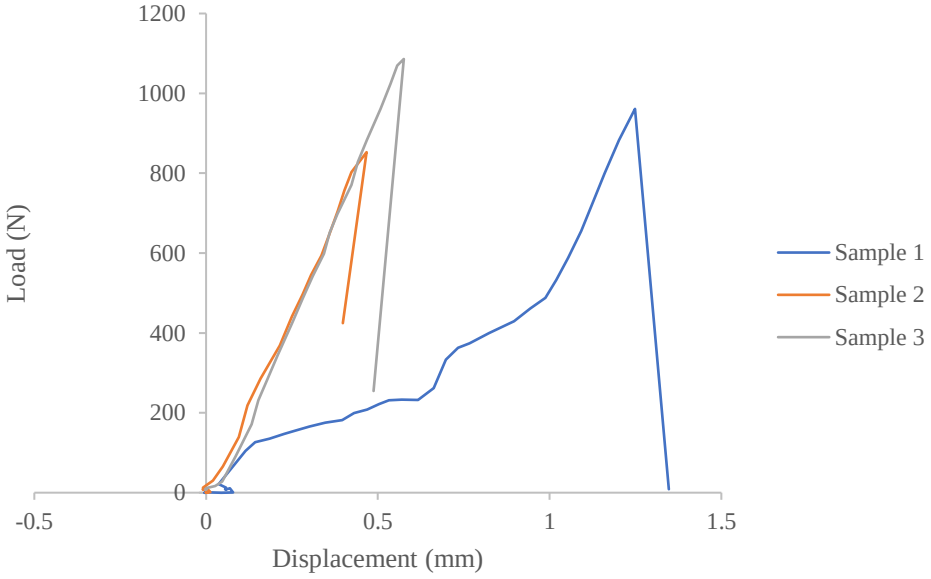

(a) Hydrocal

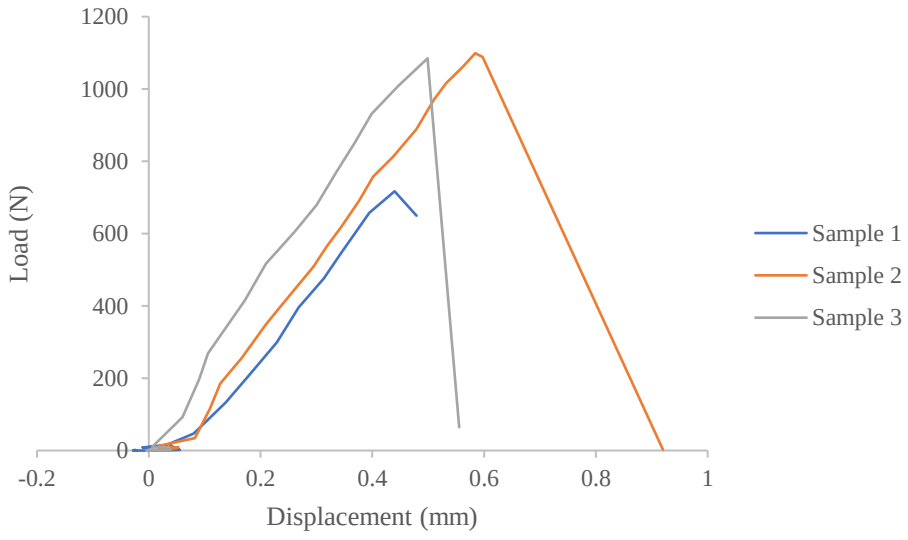

(b) Rapid Set

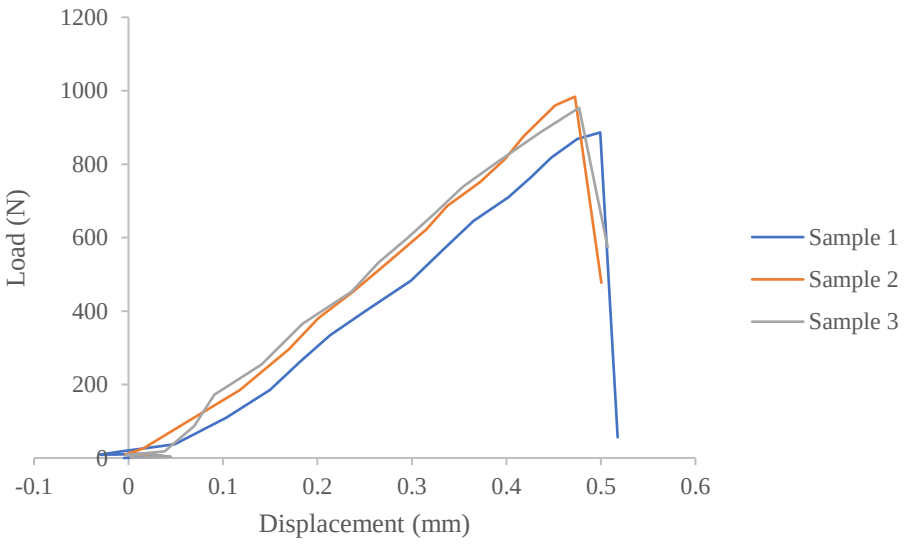

(c) Silpro TDQ

Figure 5-6: Four-point flexure test for each mortar type

The samples displayed consistency within each mortar type with two outliers. Sample 1 of the Hydrocal displayed some noise in the loading curve, as the initial slope of the curve was not consistent with the other Hydrocal samples. Sample 1 of the Rapid Set failed at a lower peak load than the other two Rapid Set samples, which is likely due to an irregularity in the AAC or an effect of weathering of the tile, since the failure occurred within the tile and not at the interface between the tile and the mortar. In fact, all failures occurred within the AAC tile, demonstrating that each of the three mortars has a sufficient bond and strength to develop the full capacity of the AAC material. The failure location, peak load, and flexural strength, calculated using Equation 5.3, are summarized in Table 5-2.

Table 5-2: Peak load and flexural strength

	Sample No.	Break in Tile? (Y/N)	Max Load, lb (N)	Flexural Strength, psi (kPa)	Average Flexural Strength, psi (kPa)
Hydrocal	1	Y	216.1 (961.1)	54.0 (372.3)	54.3 (374.4)
	2	Y	191.7 (852.7)	47.9 (330.3)	
	3	Y	244.2 (1086.1)	61.0 (420.6)	
Rapid Set	1	Y	161.2 (717.0)	40.3 (277.9)	54.3 (374.4)
	2	Y	247.0 (1098.9)	61.8 (426.1)	
	3	Y	243.9 (1084.8)	61.0 (420.6)	
Silpro TDQ	1	Y	199.3 (886.5)	49.8 (343.4)	52.9 (364.7)
	2	Y	221.2 (984.0)	55.3 (381.3)	
	3	Y	214.4 (953.9)	53.6 (369.6)	

5.3: Discussion

The results from this test show that the mortar is able to gain sufficient strength after 48 hours. The bond strength between the mortar and the tile was not the limiting factor for any of the samples, as the failure did not occur at the tile-mortar interface. The flexural strength of the bond of wet face specimens is stronger than the flexural strength of the AAC tile. Further, since all the specimens broke within the tile, the flexural strength values are conveying the flexural strength of the tile. The average flexural strength across all nine specimens is 53.9 ± 6.7 psi. The low standard deviation shows consistency among the AAC. Prior to preparation of the samples, the AAC was stored outside for many years, experiencing large fluctuations in temperatures; these results are indicative that the material is able to withstand weathering overtime.

A key question of this thesis is whether AAC tile can be used in combination with fast-setting mortar so that the tile vault can be constructed without falsework. The flexural strength of the tile, which is recorded in this chapter provides preliminary data needed to determine the maximum size of a tile that can be cantilever and supported by the mortar bond alone. Figure 5-7 shows a cantilevered tile of dimensions L x d x b (not shown). The weight of the tile W is equal to $\rho*L*d*b$, where ρ is the density of the tile. As noted by Ramage (2006), the larger the size of the tile, the shorter the construction time of the vault.

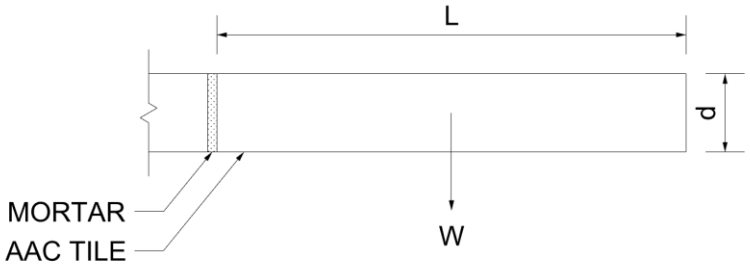

Figure 5-7: Cantilevered tile

The moment at the mortar bond induced by self-weight of the tile is defined in Equation 5.4. Based on Equation 5.2 for the maximum bending stress, the maximum cantilever length is determined in Equation 5.5.

$$M = \frac{\rho b d L^2}{2} \quad \text{Eq. 5.4}$$

$$L = \sqrt{\frac{\sigma d}{3\rho}} \quad \text{Eq. 5.5}$$

For d = two inches, the AAC tile thickness, σ = 53.9 psi, the average tile flexural strength, and ρ = 37 pcf = 0.021 lb/in^3, the AAC tile density, the maximum cantilevered tile length is found to be 41 inches.

Two important considerations must be noted. First, often during cantilevered construction, a tile is support on two edges with mortar bonds to two adjacent tiles; the assumption that the tile is only supported on a single edge, as in the calculation above, provides a conservative value for the maximum cantilever length. Secondly, the 41-inch cantilever length is calculated using 53.9 psi as the bending capacity. This is valid at 48 hours, and any other time when the strength of the tile is less than the strength of the mortar. However, at earlier time scales, when the strength of the mortar is less than the tile, the mortar strength is the critical bending capacity that must be used in Equation 5.5. Such is the case during construction, when the mortar just begins to cure and the initial set strength is less than the strength of the tile. Therefore, further testing on the flexural capacity of the mortar at shorter time scales is necessary in order to determine the maximum cantilever length of a tile during construction.

Lastly, the weight and embodied carbon calculations in Chapter 4 considered a wet mortar density of 120 pcf (USG 2021, Silpro 2021) and an ECC of 0.2 (Jones et al. 2019). The

ECC of each individual mortar was not considered; because the weight of the mortar is such a small percentage of the total weight of the system, that the choice of mortar does not greatly impact the embodied carbon of the system. Further research on the ECC of each type of mortar along with further testing will quantitatively inform which mortar performs best. The current recommendation remains USG Hydrocal, as it has already been proved as a viable mortar for vaulting with AAC by Ramage (2006), Lau (2006) and Dessi-Olive (2018).

Chapter 6 : Conclusions

6.1 Summary of Findings

This thesis shows that an AAC vaulted floor system is a lightweight, low embodied carbon alternative to conventional flat concrete slabs. Previous research on vaulted systems using concrete shells proved to be lightweight, through an efficient use of material, but expensive and labor-intensive fabrication techniques preclude these systems as viable replacements for flat slab, which requires a simpler formwork. Overall, this thesis addresses the questions posed at the onset of the study and concludes that:

- AAC has sufficient strength to serve as a structural vaulting material and to carry loads during construction.
- The concrete fill can act as a compressive load path to supply the structural depth needed for a safe structure under symmetrical and asymmetrical loads.
- The square groin vault is an ideal geometry to decrease self-weight and embodied carbon of the floor system.
- A square groin vault with lightweight, low embodied carbon fill, such as lightweight concrete with glass bubbles, offers up to 67% reduction in structural weight and a 61% reduction in embodied carbon compared to a conventional flat slab in reinforced concrete.

Chapter 2 focuses on 2D structural analysis of representative slices of the vaulted system. Studying one-foot-wide strips along the edges and the diagonal, an analysis of the thrust lines using graphic statics shows that AAC has enough strength to be used in a structural capacity under construction loads. Unlike the system designed by Hawkins (2019) where the concrete fill was only used to transfer loads from the floor to the shell, this design uses the concrete fill in place of ribs or stiffeners. The thrust line analysis showed that there exist viable load paths within the fill material to the supports under symmetrical and asymmetrical live loads during the built phase. The 2D structural analysis demonstrates that the proposed system has the stability and strength to satisfy the safe theorem and strength criterion described by Heyman (1999). The one-way action assumed in the 2D analysis produced a 20 foot by 20 foot barrel vault of one foot

rise with a total longitudinal thrust of 148 kips, which is reduced through the use of a two-way groin vault.

Chapter 3 investigates the global system to determine the most efficient way to resist the outward thrust of adjacent bays. Steel tension ties at the corner of each bay ensure that each bay is self-stabilized; the loss or removal of one bay will have no effect on the global system. The simple volume calculations detailed in this chapter provide an easy method of quantifying the amount of concrete, mortar, AAC, and steel for a vault of any span and depth. The total longitudinal thrust of the 20 foot by 20 foot groin vault of one foot rise is 122.2 kips, a 17% reduction from the 2D analysis.

The design exploration of the system in Chapter 4 builds upon these volume and rigid body thrust calculations and considers the application of the vaulted floor in the context of a full structure. Considering the normalized weight and embodied carbon from all the materials, including columns, the square groin vault with a lightweight fill affords 67% reduction in structural weight and a 61% reduction in embodied carbon compared to a conventional flat slab.

The preliminary flexure tests on three types of mortar provide quantitative data that point to the possibility of using AAC tile to build vaults without falsework. Additional testing is required in order to determine the maximum cantilever length of a tile during construction.

6.2 Future Work

This study pushes the limits of material efficiency and shows that the proposed geometry and materials are viable under symmetrical and asymmetrical gravity loads during construction and the built phase of the structure. As mentioned above, additional testing of the flexural strength of the AAC tile mortar bond is necessary to inform the maximum size of a cantilevered tile during construction, based on the strength gain of the mortar over time. An investigation into proper fire protection per building codes of the exposed steel ties is needed. Future work also entails a study of the system under lateral loading as well as vibrations and cyclic loading.

Bibliography

Alexandru, Timu, Barbuta Marinela, Dumitrescu Laura, and Baran Irina. 2019. "Mechanical and Environmental Performances of Concrete Using Recycled Materials." *Procedia Manufacturing* 32: 253–58. https://doi.org/10.1016/j.promfg.2019.02.211.

Allen, Edward, Wacław Zalewski, and Joseph Iano. 2010. *Form and Forces: Designing Efficient, Expressive Structures*. Hoboken, N.J: John Wiley & Sons, Inc.

American Institute of Steel Construction (AISC). 2017. *Steel Construction Manual*. Chicago, Ill.: American Institute of Steel Construction.

American Society of Civil Engineers (ASCE), ed. 2013. *Minimum Design Loads for Buildings and Other Structures*. ASCE Standard. Reston, Virginia: Published by American Society of Civil Engineers.

ASTM International. *C67/C67M-20 Standard Test Methods for Sampling and Testing Brick and Structural Clay Tile*. West Conshohocken, PA; ASTM International, 2020. doi: https://doi.org/10.1520/C0067_C0067M-20

ASTM International. *C496/C496M-17 Standard Test Method for Splitting Tensile Strength of Cylindrical Concrete Specimens*. West Conshohocken, PA; ASTM International, 2017. doi: https://doi.org/10.1520/C0496_C0496M-17

Bannister, Turpin C. 1968. "The Roussillon Vault: The Apotheosis of a 'Folk' Construction." *Journal of the Society of Architectural Historians* 27 (3): 163–75. https://doi.org/10.2307/988500.

Barentin, Cristián Calvo, Ioannis-Athanasios Zornatzis, Gnanli Landrou, Thibault Demoulin, Guillaume Habert, and Philippe Block. 2020. "When Low Strength Materials Meet Funicular Structures: A Sustainable Clay Floor Structure Solution for Emerging Contexts." *IOP Conference Series: Earth and Environmental Science* 588 (November): 042024. https://doi.org/10.1088/1755-1315/588/4/042024.

Beres, Attila B., and Basile G. Rabbat. 2007. "Strut-and-Tie Model for Structural Concrete Design." Portland Cement Association.

Block, Philippe. 2006. "Tutorial 3: Random/Moldable Arch." InteractiveThrust for Cabri Geometry II Plus. 2006. http://web.mit.edu/masonry/interactiveThrust/tutorials/tutorial3.pdf.

Block, Philippe, and John Ochsendorf. 2008. "Lower-Bound Analysis of Masonry Vaults." In *Structural Analysis of Historic Construction: Preserving Safety and Significance*, edited by Enrico Fodde, 593–600. CRC Press. https://doi.org/10.1201/9781439828229.ch67.

Block, Philippe, Tom van Mele, Matthias Rippmann, and Noelle C. Paulson. 2017. *Beyond Bending: Reimagining Compression Shells*. DETAIL Special. München: Edition Detail.

Block, Philippe, Thierry Ciblac, and John Ochsendorf. 2006. "Real-Time Limit Analysis of Vaulted Masonry Buildings." *Computers & Structures* 84 (29–30): 1841–52. https://doi.org/10.1016/j.compstruc.2006.08.002.

Chilton, John, and Heinz Isler. 2000. *Heinz Isler: The Engineer's Contribution to Contemporary Architecture*. London: Telford.

CTS. 2021. "Rapid Set Mortar Mix." CTS. Accessed May 9, 2021. https://www.ctscement.com/datasheet/MORTAR_MIX_Datasheet_DS_003_EN?c=&t=Professionals.

De Wolf, C., M. Ramage, and J. Ochsendorf. 2016. "Low Carbon Vaulted Masonry Structures." *Journal of the International Association for Shell and Spatial Structures* 57 (4): 275–84. https://doi.org/10.20898/j.iass.2016.190.854.

Dessi-Olive, Jonathan, Nick Krouwel, Mark West, and John Ochsendorf. 2018. "Tile Vaulting with Lightweight Concrete and Fiberglass Spline Formwork." In *IASS Symposium*. Boston.

DOE. 2015a. "A Common Definition for Zero Energy Buildings." Energy Efficiency & Renewable Energy. U.S. Department of Energy. https://www.energy.gov/sites/prod/files/2015/09/f26/bto_common_definition_zero_energy_buildings_093015.pdf.

DOE. 2015b. "Quadrennial Technology Review (QTR): An Assessment of Energy Technologies and Research Opportunities." Chapter 5: Increasing Efficiency of Building Systems and Technologies. U.S. Department of Energy. https://www.energy.gov/sites/prod/files/2017/03/f34/qtr-2015-chapter5.pdf.

Ersan, Yusuf Cagatay, Sedat Gulcimen, Tuba Nur Imis, Osman Saygin, and Nigmet Uzal. 2020. "Life Cycle Assessment of Lightweight Concrete Containing Recycled Plastics and Fly Ash." *European Journal of Environmental and Civil Engineering*, June, 1–14. https://doi.org/10.1080/19648189.2020.1767216.

Gaitan, Sabrina. 2021. "Vaulted Earthen Floor Systems for Low-Cost Housing Construction." Massachusetts Institute of Technology.

Guastavino, Rafael. 1892. "Essay on the Theory and History of Cohesive Construction Applied Especially to the Timbrel Vault." Boston:Ticknor and Co.

Hawkins, William. 2019. "Thin-Shell Concrete Floors for Sustainable Buildings." Doctor of Philosophy, University of Cambridge.

Hawkins, Will, John J. Orr, Paul Shepherd, and Tim Ibell. 2017. "Thin-Shell Textile-Reinforced Concrete Floors for Sustainable Buildings." In . Hamburg.

Heyman, Jacques. 1999. *The Stone Skeleton: Structural Engineering of Masonry Architecture*. Cambridge; New York: Cambridge University Press.

Huerta, Santiago. 2003. "The Mechanics of Timbrel Vaults: A Historical Outline." In *Essays on the History of Mechanics*, edited by Antonio Becchi, Massimo Corradi, Federico Foce, and Orietta Pedemonte, 89–134. Basel: Birkhäuser Basel. https://doi.org/10.1007/978-3-0348-8091-6_5.

Ibn-Mohammed, T., R. Greenough, S. Taylor, L. Ozawa-Meida, and A. Acquaye. 2013. "Operational vs. Embodied Emissions in Buildings—A Review of Current Trends." *Energy and Buildings* 66 (November): 232–45. https://doi.org/10.1016/j.enbuild.2013.07.026.

Jones, Craig, and Geoffrey Hammond. 2019. "Inventory of Carbon & Energy Version 3.0 (ICE DB V3.0)." Circular Ecology. https://circularecology.com/embodied-carbon-footprint-database.html.

King, Bruce. 2017. *The New Carbon Architecture: Building to Cool the Climate*. Gabriola Island, BC, Canada: New Society Publishers.

Lau, Wanda. 2006. "Equilibrium Analysis of Masonry Domes." Massachusetts Institute of Technology.

Liew, A., D. López López, T. Van Mele, and P. Block. 2017. "Design, Fabrication and Testing of a Prototype, Thin-Vaulted, Unreinforced Concrete Floor." *Engineering Structures* 137 (April): 323–35. https://doi.org/10.1016/j.engstruct.2017.01.075.

Maxwell, J. Clerk. 1864. "XLV. *On Reciprocal Figures and Diagrams of Forces*." *The London, Edinburgh, and Dublin Philosophical Magazine and Journal of Science* 27 (182): 250–61. https://doi.org/10.1080/14786446408643663.

Moya, Luis. 1947. *Bóvedas Tabicadas*. Textos Dispersos. Madrid: Colegio Oficial de Arquitectos de Madrid.

Ochsendorf, John Allen. 2010. *Guastavino Vaulting: The Art of Structural Tile*. New York: Princeton Architectural Press.

Portland Cement Association (PCA). 2019. "Autoclaved Aerated Concrete." PCA. Accessed May 9, 2021. https://www.cement.org/cement-concrete/paving/buildings-structures/concrete-homes/building-systems-for-every-need/autoclaved-aerated-concrete.

Ramage, Michael H. 2006. "Catalan Vaulting in Advanced Material: New Approaches to Contemporary Compressive Form." Master of Architecture, Massachusetts Institute of Technology

Robati, Mehdi, Timothy J. McCarthy, and Georgios Kokogiannakis. 2016. "Incorporating Environmental Evaluation and Thermal Properties of Concrete Mix Designs." *Construction*

and Building Materials 128 (December): 422–35. https://doi.org/10.1016/j.conbuildmat.2016.10.092.

Silpro. 2021. "TDQ." Silpro. Accessed May 9, 2021. https://www.silpro.com/product/tdq/.

Stuart, D. Matthew. 2007. "Antiquated Structural Systems Series." *Structure Magazine*, December. https://www.structuremag.org/?p=5925.

USG. 2021. "Hydrocal White Gypsum Cement." USG. Accessed May 9, 2021. https://www.usg.com/content/usgcom/en/products/industrial/art-statuary/hydrocal-white-gypsum-cement.html.

Wilson, Samuel. 2016. "Structural Design of Shallow Masonry Domes." Massachusetts Institute of Technology.

Yun, Tae Sup, Yeon Jong Jeong, Tong-Seok Han, and Kwang-Soo Youm. 2013. "Evaluation of Thermal Conductivity for Thermally Insulated Concretes." *Energy and Buildings* 61 (June): 125–32. https://doi.org/10.1016/j.enbuild.2013.01.043.

Appendix

A.1: Splitting Tensile Strength Test

The splitting tensile test provides additional data on the strength of each mortar tested in the four-point flexure test in Chapter 5.

A.1.1: Methodology

The second test performed is a split cylinder test, used to determine the splitting tensile strength of the different mortar types. This test is modified from ASTM C496/C496M, "Standard Test Method for Splitting Tensile Strength of Cylindrical Concrete Specimens" (ASTM 2017). In this test, cylinders are loaded in compression along the length of the cylinder, which induces tensile stress within the specimen. Because the area of load application is in triaxial compression, the specimen can withstand much greater compressive loads then tensile; thus, the specimen fails in tension. The splitting tensile strength is calculated using Equation A.1.

Mortars were prepared per Table 5-1 and cast into cylindrical plastic molds that are four inches tall and two inches in diameter. The specimens were left to cure in a dry room for 24 hours. Prior to testing, measurements of the mass, length, and diameter, measured at four different points on the cylinder, were recorded for each specimen, shown in Table A-1. A schematic of the test set up is shown in Figure A-1 and the actual test set up is shown in Figure A-2. Thin rubber strips are used to ensure the load is distributed evenly along the surface of the cylinder. The specimens were loaded at a rate of 8000 N/min.

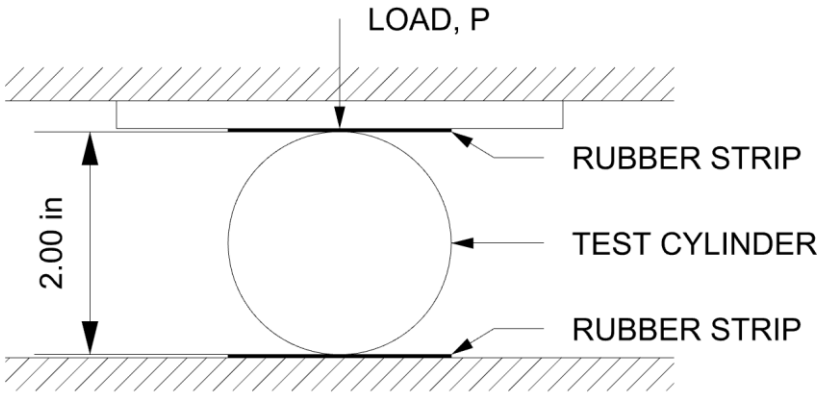

Figure A - 1: Schematic of splitting tensile test setup

Figure A - 2: Actual splitting tensile test setup

A.1.2: Results

Nine specimens were tested, three of each mortar type. Figure A-3 shows the load versus displacement plots for the three types of mortar.

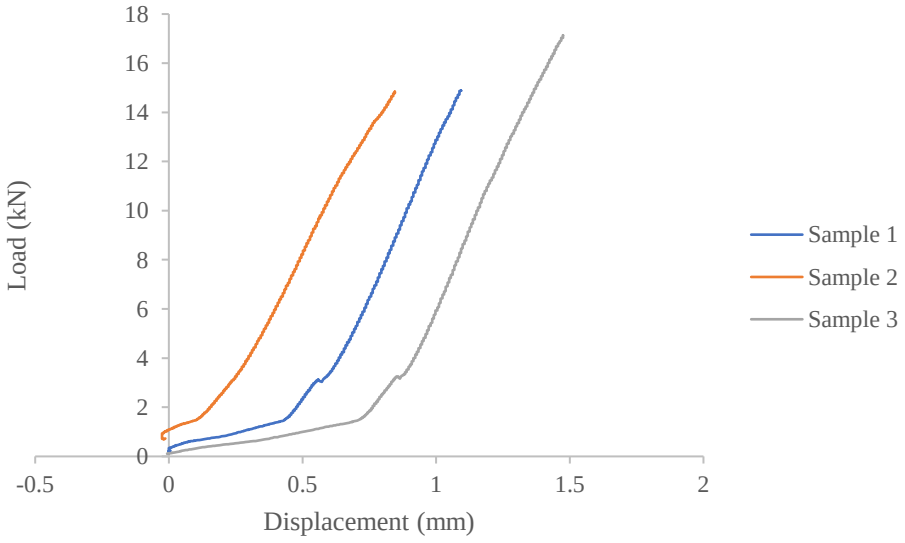

(a) Hydrocal

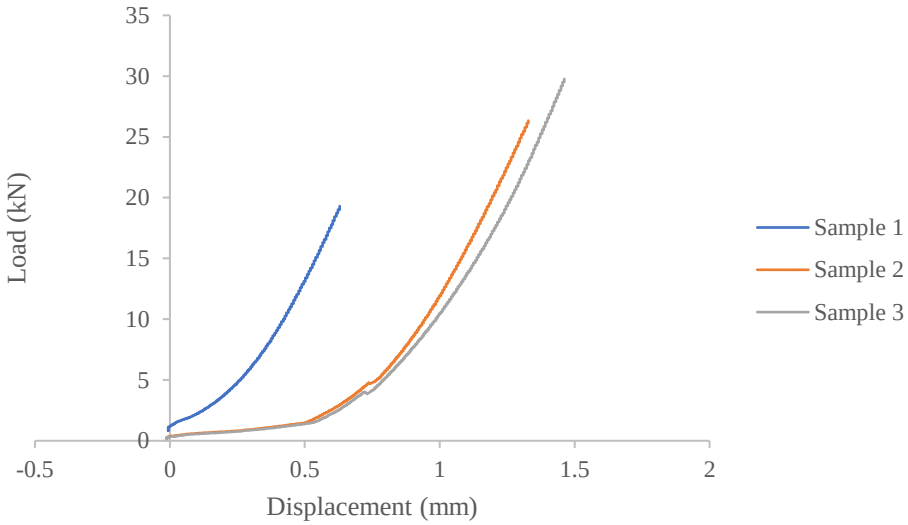

(b) Rapid Set

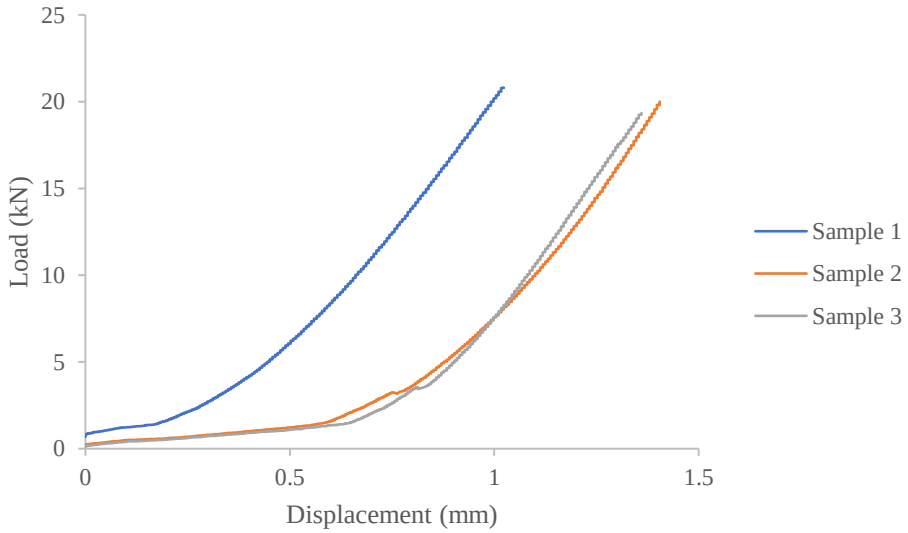

(c) Silpro TDQ

Figure A - 3: Splitting tensile test for each type of mortar

Table A.1 shows the mass, length, and diameter measurements for each specimen, as well as the peak load and splitting tensile strength. Spitting tensile strength is calculated from

Equation A.1, where T is the splitting tensile strength, P is the peak load, l is the cylinder length, and d is the average cylinder diameter.

$$T = \frac{2P}{\pi l d} \qquad \text{Eq. A.1}$$

Table A - 1: Measurements of splitting tensile test

	Sample No.	Mass, g	Average Diameter, mm	Length, mm	Peak Load, kN (k)	Splitting Tensile Strength, MPa (psi)	Average Splitting Tensile Strength, MPa (psi)
Hydrocal	1	363.5	51.09	101.56	14.9 (3.3)	1.8 (264.8)	1.9 (278.7)
	2	363.2	51.11	101.28	14.8 (3.3)	1.8 (264.6)	
	3	362.3	51.11	100.88	17.1 (3.9)	2.1 (306.8)	
Rapid Set	1	424.0	50.98	101.20	19.3 (4.3)	2.4 (345.4)	3.1 (450.6)
	2	422.9	50.91	100.95	26.3 (5.9)	3.3 (473.1)	
	3	425.3	51.03	100.96	29.8 (6.7)	3.7 (533.4)	
Silpro TDQ	1	422.6	51.01	101.06	20.8 (4.7)	2.6 (372.5)	2.5 (357.9)
	2	428.9	51.02	101.98	20.0 (4.5)	2.4 (354.9)	
	3	426.8	51.12	100.86	19.3 (4.3)	2.4 (346.2)	